LJMU Research Online

Malkeson, SP, Ahmed, U, Turquand d'Auzay, C, Pillai, AL, Chakraborty, N and Kurose, R

Displacement speed statistics in an open turbulent jet spray flame

http://researchonline.ljmu.ac.uk/id/eprint/13913/

Article

For more information please contact researchonline@ljmu.ac.uk

1

Displacement Speed statistics in an Open Turbulent Jet Spray Flame

4

5 S.P. Malkeson [a]*, U. Ahmed [b], C. Turquand d'Auzay [b,c], A. L. Pillai [d], N. Chakraborty [b],

6 Ryoichi Kurose [d]

7 [a] Department of Maritime and Mechanical Engineering, Liverpool John Moores University,

8 Liverpool, L3 3AF, United Kingdom

9 [b] School of Engineering, Newcastle University, Newcastle-Upon-Tyne, NE1 7RU, United

10 Kingdom

11 [c] Ricardo Ltd., Shoreham Technical Centre, Old Shoreham Rd., Shoreham-by-Sea, BN43

12 5FG, United Kingdom

13 [d] Department of Mechanical Engineering and Science, Kyoto University, Kyoto, 606-8501,

14 Japan

15

16 * Corresponding author: S.P.Malkeson@ljmu.ac.uk

17 Phone No: +44 (0)151 904 1403

18 **ABSTRACT**

19 In this study, a three-dimensional Direct Numerical Simulation of an open turbulent jet spray

20 flame has been used to investigate the statistical behaviour of displacement speed S_d and its

21 components to provide physical explanations for the observed behaviours at different axial

22 locations downstream of the jet exit. The open turbulent jet spray flame exhibits fuel-lean

23 conditions close to the jet exit but fuel-rich conditions have been observed further downstream

24 due to the evaporation of fuel droplets. For the axial locations considered, combustion takes

25 place under low Damköhler number conditions. The displacement speed of reaction progress

26 variable isosurfaces shows qualitatively similar behaviour for all axial locations considered –

27 predominantly positive across the major part of the flame but with small, potentially negative,

28 values towards the burned-gas-side. The components of displacement speed arising from

29 chemical reaction rate and flame normal molecular diffusion remain leading order contributors

30 and the competition between these determines the mean behaviour of displacement speed.

31 These observations are consistent with studies of turbulent spray flames in canonical

32 configurations and low Damköhler number turbulent premixed and stratified flames. This

33 suggests that flow geometry in the absence of mean curvature might not be important in

34 determining the mean behaviour of displacement speed and its components. Therefore, the

35 modelling methodologies employed for turbulent stratified flames can potentially be extended

36 for turbulent spray flames. However, the modelling methodologies, which implicitly assume

37 equality between the surface-weighted values of density-weighted displacement speed and

38 local laminar burning velocity, might be rendered invalid for turbulent spray flames.

39

40 **Keywords:** Turbulent droplet combustion; Open turbulent jet; Spray flame; Mixture Fraction;

41 Displacement Speed

1. INTRODUCTION

The combustion of droplet-laden mixtures plays an important role in a number of engineering applications, ranging from Internal Combustion engines (e.g. Compression Ignition and Direct Injection engines) [1,2] to aero gas turbines [2,3] to explosion hazards [4]. In such engineering applications, the fuel is typically delivered into the combustion chamber as a cloud of liquid droplets or as a spray, and the properties of this cloud or spray will have significant influence on the efficiency of combustion, power output and the formation of pollutants. Despite the applicability of the combustion of droplet-laden mixtures, it has been given relatively limited consideration in comparison to the vast body of literature on premixed, non-premixed, partially-premixed and stratified flames. However, a greater level of understanding of turbulent spray combustion is essential for the development of future generations of higher-efficiency, lower-emission combustion devices and to ensure greater control of industrial processes involving spray combustion.

Significant insights into the behaviour of the combustion of turbulent droplet-laden mixtures through both experimental [5-14] and numerical [14-27] investigations have been obtained. Furthermore, recently several Direct Numerical Simulations (DNS) analyses [19-21,24-27] focussed on the flame propagation statistics in turbulent droplet-laden mixtures in canonical configurations. In these analyses [19-21,24-27], the statistical behaviours of the displacement speed of the reaction progress variable c have been analysed, providing important information with respect to modelling methodologies in turbulent spray flames. These statistics of displacement speed are fundamentally important for flame surface area evolution [28] and both level-set [29], and Flame Surface Density (FSD) [28] based approaches of turbulent reaction rate closure. However, the effects of mean shear were absent in the configurations analysed in [19-21,24-27] and thus it is worthwhile to analyse the flame propagation in a configuration with mean shear, which is typical of laboratory and industrial scale burners. Several recent analyses concentrated on displacement speed statistics of turbulent premixed flames in a laboratory-scale burner [30-32] and canonical configurations [33] based on high-fidelity simulations but such an analysis is yet to be carried out for turbulent spray flames. To the best of the authors' knowledge, the analysis of the flame propagation behaviour in the combustion of turbulent droplet-laden mixtures is yet to be considered in detail for an open turbulent jet spray flame [22,23], which is representative of a laboratory-scale experimental configuration [14]. Such an analysis would offer important insights with regards to the propagation behaviour of turbulent spray flames in realistic configurations, which are currently not available.

75   The current analysis builds upon the existing literature of flame propagation into droplet-laden

76   mixtures [19-21,24-27] by considering an open turbulent jet spray flame [22,23], analysing the

77   behaviour of the density-weighted displacement speed S_d^* and its components at different axial

78   locations of the spray flame. The main objectives of the current study are:

79   (i)   To identify and provide explanations for the statistical behaviours of the density-

80   weighted displacement speed S_d^* of the reaction progress variable c, and its components

81   in the context of an open turbulent jet spray flame.

82   (ii)   To provide modelling implications for displacement speed statistics in turbulent droplet

83   combustion.

84   The remainder of the paper is organised as follows. The next section discusses the relevant

85   mathematical background and numerical implementation for the current study. Following this,

86   the results are presented and, subsequently, discussed. Finally, the main findings are

87   summarised, and conclusions are drawn.

88

89   2. MATHEMATICAL BACKGROUND & NUMERICAL IMPLEMENTATION

90   2.1 Relevant mathematical background

91   In the current analysis, the DNS data analysed has been obtained by Pillai and Kurose [22,23]

92   using the FK[3] code [22,23,34-42]. The liquid spray fuel is Ethanol (C_2H_5OH) and a two-step

93   global reaction mechanism with 6 species (C_2H_5OH, O_2, CO_2, H_2O, N_2 and CO) is considered

94   for representing combustion process [43] to ensure computational economy. This reaction

95   mechanism was developed by modifying the reaction rate parameters and provides good

96   reproducibility of experimentally measured flame speeds in fuel-air mixtures whilst being able

97   to predict lean and rich flammability limits, flame temperature and burned gas composition

98   with good accuracy across a range of equivalence ratios [43]. The two-step global chemistry

99   can be represented in the following manner:

100    $$C_2H_5OH + 2O_2 \xrightarrow{k_1} 2CO + 3H_2O \tag{1}$$

101    $$CO + \frac{1}{2}O_2 \underset{k_{-2}}{\overset{k_2}{\rightleftarrows}} CO_2 \tag{2}$$

where k_1 is the reaction rate of Ethanol oxidisation in Eq. 1 and k_2 is the rate of forward reaction for CO oxidisation in Eq. 2. The reaction rates are given as modified Arrhenius expressions [43] in the following manner [43]:

$$k_1 = 1.8 \times 10^{12} . exp\left(\frac{-30}{RT}\right)[C_2H_5OH]^{0.15}[O_2]^{1.6} \tag{3}$$

$$k_2 = 10^{14.6} . exp\left(\frac{-40}{RT}\right)[CO]^1[H_2O]^{0.5}[O_2]^{0.25} \tag{4}$$

In Eq. 2, the reverse reaction k_{-2} is defined as [43]:

$$k_{-2} = 5 \times 10^8 . exp\left(\frac{-40}{RT}\right)[CO_2]^1 \tag{5}$$

The terms in the square brackets of Eqs. 3-5 represent the molar concentrations ($moles.m^{-3}$) of different chemical species. The molar concentration of $[X_k]$ of the kth species is given as:

$$[X_k] = [\rho Y_k / W_k] \tag{6}$$

where W_k is the molecular weight of the kth species. The two-step global reaction mechanism used in the current analysis provides a more accurate representation of the flame parameters compared to a one-step global reaction mechanism [43].

In the current study, the carrier gas-phase is treated as a Eulerian continuum and the dispersed fuel droplets are tracked as Lagrangian mass points. The gas phase is solved using a Eulerian framework and the governing equations considered for mass, momentum, energy and species mass fraction in the following manner:

$$\frac{\partial \rho}{\partial t} + \frac{\partial(\rho u_i)}{\partial x_i} = S_\rho \tag{7}$$

$$\frac{\partial(\rho u_i)}{\partial t} + \frac{\partial(\rho u_i u_j)}{\partial x_j} = -\frac{\partial p}{\partial x_i} + \frac{\partial \tau_{ij}}{\partial x_j} + S_{\rho u} \tag{8}$$

$$\frac{\partial \rho h}{\partial t} + \frac{\partial(\rho h u_j)}{\partial x_j} = \frac{\partial p}{\partial t} + u_j \frac{\partial p}{\partial x_j} + \frac{\partial}{\partial x_j}\left(\rho D_h \frac{\partial h}{\partial x_j}\right) + \tau_{ij}\frac{\partial u_i}{\partial x_j} + S_{rad} + S_{\rho h} \tag{9}$$

$$\frac{\partial \rho Y_k}{\partial t} + \frac{\partial(\rho Y_k u_j)}{\partial x_j} = \frac{\partial}{\partial x_j}\left(\rho D_k \frac{\partial Y_k}{\partial x_j}\right) + S_{comb,k} + S_{\rho Y_k} \tag{10}$$

Equations 7-10 are considered alongside the equation of state for an ideal gas. In Eqs. 7-10, ρ is the density, u is the gas-phase velocity, p is the pressure, τ_{ij} is the stress tensor, h is the specific enthalpy, Y_k is the mass fraction of the kth chemical species, S_{rad} is the source term for radiative heat loss, $S_{comb,k}$ is the source term due to combustion reaction, and D_h and D_k

127   are the gaseous thermal diffusivity and mass diffusion coefficient of kth species, respectively,

128   which are defined as:

129     $$D_h = \frac{\lambda}{\rho c_p}$$ (11)

130     $$D_k = \frac{\lambda}{\rho c_p}$$ (12)

131   where λ is the thermal conductivity, c_p is the specific heat and unity Lewis number conditions

132   (i.e. $Le = 1.0$) are considered. It should be noted that the phase coupling between the carrier

133   gas-phase and dispersed-phase (i.e. fuel droplets) is achieved using the Particle-Source-In-Cell

134   (PSI-Cell) approach [44]. The PSI-Cell approach considers each computational cell as a control

135   volume and each fuel droplet is considered as a source of mass, momentum and energy to the

136   gas-phase. As the fuel droplets evaporate and pass through the cell, the change in their mass,

137   momentum and energy are considered as a source/sink to the gas-phase mass, momentum and

138   energy, respectively. This is achieved through the source terms S_ρ, $S_{\rho u}$, $S_{\rho h}$ and $S_{\rho Y_k}$ found in

139   Eqs. 7-10 and these represent the interactions between the gas-phase and dispersed-phase,

140   allowing two-way coupling between the two phases. The source terms S_ρ, $S_{\rho u}$, $S_{\rho h}$ and $S_{\rho Y_k}$

141   are defined in the following manner:

142     $$S_\rho = -\frac{1}{\Delta V} \sum_N \frac{dm_d}{dt}$$ (13)

143     $$S_{\rho u} = -\frac{1}{\Delta V} \sum_N \frac{dm_d \vec{u}_d}{dt}$$ (14)

144     $$S_{\rho h} = -\frac{1}{\Delta V} \sum_N \frac{dm_d h_d}{dt}$$ (15)

145     $$S_{\rho Y_k} = -\frac{1}{\Delta V} \sum_N \frac{dm_d}{dt} \text{ for fuel } (k = F), 0 \text{ for other species } (k \neq F)$$ (16)

146   In Eqs. 13-16, ΔV is the volume of each control volume (i.e. each computational grid cell) for

147   the gas phase calculation, m_d is the fuel droplet mass, $\vec{u}_d$ is the droplet velocity, h_d is the

148   specific enthalpy of a fuel droplet and N is the number of fuel droplets within a control volume.

149   A non-equilibrium Langmuir-Knudsen evaporation model [45-48] is considered for the

150   evaporation of the fuel droplets as the non-equilibrium effects become significant for droplet

151   diameter $d_d < 50\mu m$ [47]. In the current study, the spray flame is dilute as the volumetric

152   loading of droplets is small and, therefore, the collisions and coalescence of droplets is

153   neglected. A Lagrangian framework [34,35,46-48] is considered which individually tracks the

154 evaporating fuel droplets of the dispersed phase by solving the equations for droplet position

155 $\vec{x}_d$, droplet mass m_d, droplet velocity $\vec{u}_d$ and droplet temperature T_d in the following manner:

156
$$\frac{d\vec{x}_d}{dt} = \vec{u}_d \tag{17}$$

157
$$\frac{dm_d}{dt} = -\left(\frac{Sh}{3Sc}\right)\frac{m_d}{\tau_d}\ln(1 + B_M) \tag{18}$$

158
$$\frac{d\vec{u}_d}{dt} = \frac{f_1}{\tau_d}(\vec{u}(\vec{x}_d, t) - \vec{u}_d) + g \tag{19}$$

159
$$\frac{dT_d}{dt} = \left(\frac{Nu}{3Pr}\right)\left(\frac{c_p}{c_{p,d}}\right)\left(\frac{f_2}{\tau_d}\right)(T - T_d) + \frac{1}{m_d}\left(\frac{dm_d}{dt}\right)\frac{L_V}{c_{p,d}} \tag{20}$$

160 where Sh is the Sherwood number, Sc is the Schmidt number, B_M is the Spalding mass transfer

161 number, Nu is the Nusselt number, Pr is the Prandtl number, T is the gas-phase temperature,

162 c_p is the specific heat of the gas mixture, $c_{p,d}$ is the specific heat of a fuel droplet, g is the

163 gravitational acceleration and the latent heat of vaporisation L_V at T_d is calculated as:

164
$$L_V = L_{V,T_{BL,atm}}\left(\frac{T_{CL} - T_d}{T_{CL} - T_{BL,atm}}\right)^{0.38} \tag{21}$$

165 where $L_{V,T_{BL,atm}}$ is the latent heat of vaporisation at atmospheric pressure, T_{CL} is the critical

166 temperature of the fuel and $T_{BL,atm}$ is the boiling point of fuel at atmospheric pressure. In Eq.

167 18, the droplet response time τ_d is calculated by:

168
$$\tau_d = \frac{\rho_d d_d^2}{18\mu} \tag{22}$$

169 where d_d is the droplet diameter, ρ_d is the fuel droplet density and μ is the gas-phase dynamic

170 viscosity. The gas-phase Prandtl and Schmidt numbers, Nusselt and Sherwood numbers are

171 defined in the following manner:

172
$$Pr = \frac{\mu c_p}{\lambda} \tag{23}$$

173
$$Sc = \frac{\mu}{\rho D_k} \tag{24}$$

174
$$Nu = 2.0 + 0.552Re_{sl}^{1/2}.Pr^{1/3} \tag{25}$$

175
$$Sh = 2.0 + 0.552Re_{sl}^{1/2}.Sc^{1/3} \tag{26}$$

176 where Re_{sl} is the droplet Reynolds number which is based on the slip velocity $U_{sl} =$

177 $|\vec{u}(\vec{x}_d, t) - \vec{u}_d|$ and is given as:

178    $$Re_{sl} = \frac{\rho U_{sl} d_d}{\mu} \qquad (27)$$

179   In Eqs. 19 and 20, the quantities of f_1 and f_2 are the corrections for Stokes drag and heat transfer

180   for evaporating fuel droplets, respectively [15,16,36,47]. In Eq. 18, the Spalding mass transfer

181   number B_M is given by:

182    $$B_M = \frac{Y_{F,s} - Y_F}{1 - Y_{F,s}} \qquad (28)$$

183   where Y_F is the mass fraction of the fuel vapor on the far-field condition for the droplets (N.B.

184   the same condition is used for u_i and T) and $Y_{F,s}$ is the fuel vapour mass fraction on the droplet

185   surface given as:

186    $$Y_{F,s} = \frac{X_{F,s}}{X_{F,s} + (1 - X_{F,s}) W_{avg}/W_F} \qquad (29)$$

187    $$X_{F,s} = \frac{p_{sat}}{p} - \left(\frac{2L_k}{d_d}\right)\beta \qquad (30)$$

188   where p_{sat} is the saturated vapour pressure, W_{avg} is the average molecular weight of the gas

189   mixture, W_F is the molecular weight of the fuel vapour, $X_{F,s}$ is the fuel vapour mole fraction at

190   the droplet surface, for which the non-equilibrium effects are accounted using the Langmuir-

191   Knudsen evaporation law [45-47]. In Eq. 30, L_K is the Knudsen layer thickness and β is the

192   nondimensional evaporation parameter given as [46,47]:

193    $$L_K = \frac{\mu[2\pi T_d (R/W_F)]^{1/2}}{Sc.p} \qquad (31)$$

194    $$\beta = -\left(\frac{\rho_d Pr}{8\mu}\right)\frac{d(d_d^2)}{dt} \qquad (32)$$

195   where R is the universal gas constant ($R = 8.314 J.mol^{-1}.K^{-1}$). It should be noted that the

196   source term S_{rad} in Eq. 9 accounts for the radiative heat loss rate per unit volume. It is modelled

197   using an optically thin approximation [49,50] of radiative heat transfer between a fluid element

198   in the flame and the cold surroundings. The radiative loss S_{rad} is approximated as:

199    $$S_{rad} = 4\sigma(T^4 - T_b^4)\left[\sum_k p_k a_{pk}\right] \qquad (33)$$

200   where $\sigma = 5.669 \times 10^{-8} W.m^{-2}.K^{-4}$ is the Stefan-Boltzmann constant, T is the gas-phase

201   temperature, T_b is the background temperature and is assumed to be $300K$, p_k is the partial

202   pressure of the kth species and $a_{p,k}$ is the Planck mean absorption coefficient of the kth

203   species. The Planck mean absorption coefficient have been calculated using RADCAL [49]

204 and the curve fits for $a_{p,k}$ for the radiating species considered in this model (i.e. CO_2, H_2O and

205 CO) are given as polynomial functions of temperature [49].

206

207 The evaporation of droplets leads to the creation of mixture inhomogeneities that can be

208 characterised by the mixture fraction ξ, which, for the current study, can be defined as [51]:

209
$$\xi = \frac{\beta - \beta_O}{\beta_f - \beta_O} \tag{34}$$

210 where $\beta_f = 6.0/W_{C_2H_6O}$, $\beta_O = -Y_{O\infty}/W_O$ and $\beta = 2Y_C/W_C + 0.5Y_H/W_H - Y_{O\infty}/W_O$; Y_m is

211 the mass fraction of species m and W_α is the molar mass of element α. It is possible to define

212 a reaction progress variable c that is based on the oxidiser mass fraction following several

213 previous analyses [19-21,24-27,52,53]:

214
$$c = \frac{(1-\xi)Y_{O_2\infty} - Y_{O_2}}{(1-\xi)Y_{O_2\infty} - Y_{O_2}^{Eq}} \tag{35}$$

215 where Y_{O_2} is the oxygen mass fraction, $Y_{O_2\infty}$ is the oxygen mass fraction in the pure oxidiser

216 stream and $Y_{O_2}^{Eq}$ is the equilibrium oxidiser mass fraction (i.e. $Y_{O_2}^{Eq} = f(Y_{O_2}, \xi)$).

217 From Eq. 35, it is possible to derive a transport equation of the reaction progress variable c

218 based on the transport equations of the oxygen mass fraction Y_{O_2} and the mixture fraction ξ as

219 [20,21,27]:

220
$$\rho \frac{\partial c}{\partial t} + \rho u_j \frac{\partial c}{\partial x_j} = \nabla \cdot (\rho D \nabla c) + \dot{\omega}_c + \dot{S}_{ev} + \dot{S}_c \tag{36}$$

221 where D is the progress variable diffusivity. The first term on the right-hand-side of Eq. 36

222 arises due to molecular diffusion, the second term represents the reaction rate, the third term is

223 the source/sink term arising due to droplet evaporation, and the final term is the cross-scalar

224 dissipation term arising due to reactant inhomogeneity [20,21,27,54,55]. The cross-scalar

225 dissipation term $\dot{S}_c$ in Eq. 36 arises due to mixture inhomogeneity, which in the current case

226 exists due to droplet evaporation [20,27]. According to the definition of c (see Eq. 35), the

227 definitions of $\dot{\omega}_c$, $\dot{S}_{ev}$ and $\dot{S}_c$ depend on the local value of mixture fraction ξ. The reaction rate

228 of the reaction progress variable $\dot{\omega}_c$ can be expressed as [20,21,24-27]:

$$229 \qquad \dot{\omega}_c = \begin{cases} -\dfrac{\xi_{st}\dot{\omega}_{O_2}}{\left[\xi(1-\xi_{st})Y_{O_2\infty}\right]} & , \ \xi \leq \xi_{st} \\[2mm] -\dfrac{\dot{\omega}_{O_2}}{\left[(1-\xi)Y_{O_2\infty}\right]} & , \ \xi > \xi_{st} \end{cases} \qquad (37)$$

230   The expressions for $\dot{S}_{ev}$ and $\dot{S}_c$ are given as [20,21,27]:

$$231 \qquad \dot{S}_{ev} = \begin{cases} \dfrac{-\xi_{st}}{\left[\xi^2(1-\xi_{st})Y_{O_2\infty}\right]}\left(\xi\dot{S}_O + \left(Y_{O_2\infty} - Y_{O_2}\right)\dot{S}_\xi\right) & , \ \xi \leq \xi_{st} \\[2mm] \dfrac{-1}{\left[(1-\xi_{st})^2 Y_{O_2\infty}\right]}\left((1-\xi)\dot{S}_O + Y_{O_2}\dot{S}_\xi\right) & , \ \xi > \xi_{st} \end{cases} \qquad (38)$$

$$232 \qquad \dot{S}_c = \begin{cases} \dfrac{2\rho D}{\xi}\nabla c \cdot \nabla\xi & , \ \xi \leq \xi_{st} \\[2mm] \dfrac{-2\rho D}{(1-\xi)}\nabla c \cdot \nabla\xi & , \ \xi > \xi_{st} \end{cases} \qquad (39)$$

233   where $\dot{S}_\xi = \left(\dot{S}_F - \dot{S}_O/s\right)/\left(Y_{F\infty} - Y_{O_2\infty}/s\right)$ is the droplet source/sink term in the mixture

234   fraction transport equation and $\dot{S}_F = (1 - Y_F)S_\rho$ and $\dot{S}_O = -Y_{O_2}S_\rho$ are the droplet source/sink

235   terms in the fuel and oxygen transport equations, respectively.

236   The molecular diffusion term (i.e. the first term on the right-hand-side) in Eq. 36 can be split

237   into its normal and tangential components to give the following [56,57]:

$$238 \qquad \nabla \cdot (\rho D \nabla c) = \vec{N} \cdot \nabla\left(\rho D \vec{N} \cdot \nabla c\right) - 2\rho D \kappa_m |\nabla c| \qquad (40)$$

239   where $\vec{N} = -\nabla c/|\nabla c|$ is the flame normal vector, $\kappa_m = 0.5\left(\nabla \cdot \vec{N}\right)$ is the arithmetic mean of

240   the two principal curvatures of a given iso-surface $c = c^*$. It should be noted that the first term

241   on the right-hand-side of Eq. 40 provides the component of the molecular diffusion normal to

242   the flame front and the second term gives the tangential molecular diffusion component.

243   The transport equation of c can be rewritten in the kinematic form as [20,21,27]:

$$244 \qquad \frac{\partial c}{\partial t} + u_j \frac{\partial c}{\partial x_j} = S_d |\nabla c| \qquad (41)$$

245   where S_d is the displacement speed which is the speed at which a given reaction progress

246   variable c iso-surface moves normal to itself with respect to an initially coincident material

247   surface. Comparing Eqs. 36 and 41 gives [20,21,27]:

$$248 \qquad S_d = \frac{\nabla \cdot (\rho D \nabla c) + \dot{\omega}_c + \dot{S}_c + \dot{A}_c}{\rho|\nabla c|} = \frac{\vec{N} \cdot \nabla\left(\rho D \vec{N} \cdot \nabla c\right) - 2\rho D \kappa_m |\nabla c| + \dot{\omega}_c + \dot{S}_c + \dot{A}_c}{\rho|\nabla c|} \qquad (42)$$

249   This can be rewritten in the following manner [20,21,27]:

10

250
$$S_d = \underbrace{\frac{\vec{N}\cdot\nabla(\rho D\vec{N}\cdot\nabla c)}{\rho|\nabla c|}}_{S_n} - \underbrace{\frac{2\rho D\kappa_m|\nabla c|}{\rho|\nabla c|}}_{S_t} + \underbrace{\frac{\dot{\omega}_c}{\rho|\nabla c|}}_{S_r} + \underbrace{\frac{\dot{S}_{ev}}{\rho|\nabla c|}}_{S_{ev}} + \underbrace{\frac{\dot{S}_c}{\rho|\nabla c|}}_{S_c} \qquad (43)$$

251 Furthermore, as displacement speed is affected by thermal expansion through its density
252 dependence, it is worthwhile to consider the density-weighted displacement speed S_d^* as it is
253 often needed for the modelling purposes [20,21,27,56,57]:

254
$$S_d^* = \underbrace{\frac{\vec{N}\cdot\nabla(\rho D\vec{N}\cdot\nabla c)}{\rho_0|\nabla c|}}_{S_n^*} - \underbrace{\frac{(2\rho D\kappa_m)}{\rho_0}}_{S_t^*} + \underbrace{\frac{\dot{\omega}_c}{\rho_0|\nabla c|}}_{S_r^*} + \underbrace{\frac{\dot{S}_{ev}}{\rho_0|\nabla c|}}_{S_{ev}^*} + \underbrace{\frac{\dot{S}_c}{\rho_0|\nabla c|}}_{S_c^*} \qquad (44)$$

255 where ρ_0 is the unburned reactant density. Accordingly, the statistical behaviours of the terms
256 $\vec{N}\cdot\nabla(\rho D\vec{N}\cdot\nabla c)$, $(-2\rho D\kappa_m|\nabla c|)$, $\dot{\omega}_c$, $\dot{S}_{ev}$ and $\dot{S}_c$ and their combined contributions will be
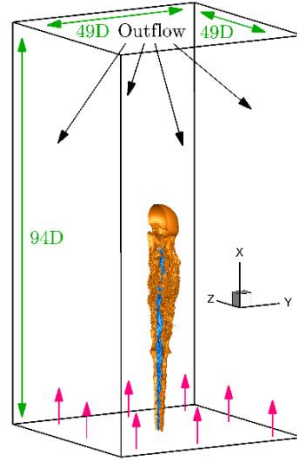257 discussed in detail in Section 3 of this paper.

258

259 **Fig. 1:**   Schematic of the computational domain and Direct Numerical Simulation set-up. The central
260   blue surface represents the spray droplet injection whereas the orange represents the annular
261   pilot. The pink arrows represent the co-flow.

262

263 **2.2 Considered DNS case and computational configuration**

264 In the current analysis, the DNS configuration corresponds to the experimental study of the
265 Ethanol spray EtF3 flame of Gounder et al. [14]. The configuration of the EtF3 flame is shown
266 schematically in Fig. 1. The spray and carrier gas are injected from a central jet nozzle ($D_j = $
267 $10.5mm$) with a bulk velocity $U_j = 24 m.s^{-1}$ surrounded by a coaxial pilot annulus ($U_p = $
268 $11.6 m.s^{-1}$ and $T_p = 2493K$) and an air co-flow ($U_c = 4.5 m.s^{-1}$). The pilot is composed of
269 the fully burned products of a stoichiometric mixture of 5.08% Acetylene (C_2H_2), 10.17%
270 Hydrogen (H_2) and 84.75% air by volume. This pilot provides the heat necessary for the

11

271 evaporation of the liquid fuel droplets. The flame is stabilised in the shear layer that is formed
272 between the inner jet and the pilot streams. The mass flow rate of liquid Ethanol in the jet is 45
273 g/min. However, amongst the polydisperse droplets formed by the nebulizer, some of the
274 droplets evaporate before reaching the exit of the nozzle and, thus, explains the presence of
275 partially gaseous fuel in the jet. The Ethanol mass flow rates at the nozzle exit are 14.3 g/min
276 for the gaseous phase and 30.7 g/min for the liquid droplets, giving a gaseous equivalence ratio
277 of 0.85. These parameters are summarised in Tables 1 and 2 for both the inner jet, pilot and co-
278 flow jet streams.

279 **Table 1:** Flow parameters for central jet at burner exit [21-24]

Flame Designation	Etf3
Fuel	Ethanol
Jet Diameter (D_j) [mm]	10.5
Bulk Jet Velocity (U_j) [$m.s^{-1}$]	24
Bulk Coflow Stream Velocity (U_c) [$m.s^{-1}$]	4.5
Carrier air mass flow rate [$g.min^{-1}$]	150
Liquid Fuel Injection Rate [$g.min^{-1}$]	45
Measured liquid flow at exit [$g.min^{-1}$]	30.7
Vapour fuel flow rate at exit [$g.min^{-1}$]	14.3
Kinematic viscosity (ν) [$m^2.s^{-1}$]	1.279×10^{-5}
Jet Reynolds number, $Re = U_j D_j/\nu$ [$-$]	19,700
Jet Mach number, $M = U_j/c_\infty$ [$-$]	0.07
Equivalence ratio at jet exit, ϕ_j [$-$]	0.85
Initial droplet and ambient temperature (T_0) [K]	293.15

280

281

282

283

284

285

Table 2: Flow parameters for annular pilot at burner exit [21-24]

Flame Designation	Etf3
Fuel	Acetylene (C_2H_2) + Hydrogen (H_2) + Air
Pilot Diameter (D_p) [mm]	25
Bulk Pilot Velocity, burned (U_p) [$m.s^{-1}$]	11.6
Pilot temperature (T_p) [K]	2493
Pilot composition ($Y_{CO_2}:Y_{H_2O}:Y_{N_2}$)	(0.1722 : 0.10575 : 0.722)

287

(a)

(b)
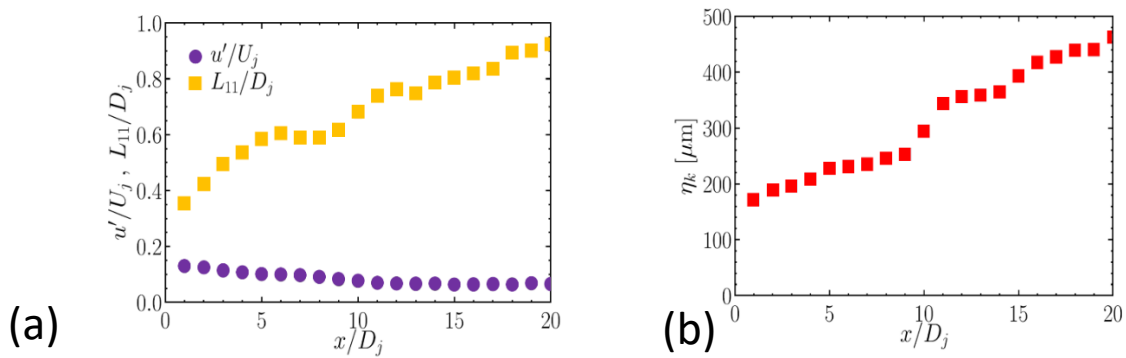
288

Fig. 2: The evolution of (a) the turbulence intensity u'/U_j and normalised integral length scale L_{11}/D_j, and (b) Kolmogorov length scale η_k along the shear layer.

291

A polydisperse spray with a distribution of diameters matching that of the experiment [14] is injected with droplet diameters ranging from 1 μm to 80 μm, with the most probable diameter being about $20\mu m$. In the current study, both the collisions and break-up have been neglected, since it is a dilute spray flame, with an inflow droplet volume fraction of about 5×10^{-4}. The droplet spray is generated by an ultrasonic nebulizer situated inside the burner, $215mm$ upstream of the exit plane [14]. Therefore, it is likely that the secondary atomization occurs inside the central jet tube of the burner, in which case the probability density function (PDF) of droplet size distribution imposed as the inflow boundary condition at the exit plane in the DNS should be sufficient, since further secondary atomization effects can be neglected. Moreover, no evidence of secondary atomization has been provided experimentally, hence it was not accounted for in the DNS. A recent analysis [58] also compared the combustion of polydisperse droplets in a two-dimensional free jet simulated using either a carrier phase DNS with point source or a fully Eulerian phase-DNS where good agreement was found when comparing the gaseous fuel mass fraction fields.

306

307 For the simulation considered in this work, a domain of $94D_j \times 49D_j \times 49D_j$ (where D_j is the

308 nozzle diameter) is used and is discretised by a non-uniform Cartesian grid of size

309 $1160 \times 400 \times 400$. A large stretching is applied in all directions towards the boundaries to

310 form absorbing zones that minimize reflection and contamination of the acoustic field near the

311 jet [22,23]. The minimum cell size needs to be larger than the droplet size to capture

312 evaporation accurately which is due to the coupling strategy between the Eulerian and

313 Lagrangian phases. In order to guarantee an appropriate resolution of both the turbulence and

314 the premixed flame front, the smallest cell size at the nozzle exit is $\Delta x = 150 \mu m$. For interested

315 readers, further details on the boundary conditions and computational grid can be found in

316 [22,23,39]. The integral length-scale and velocity fluctuations are evaluated within the shear

317 layer and are reported in Fig. 2a. As expected, the turbulence intensity decreases and the

318 integral length scale increases due to the decay of turbulence in the downstream direction. The

319 evolution of Kolmogorov length scale η_k is also reported in Fig. 2b, where it can be seen that

320 the Kolmogorov length scale η_k increases continuously downstream from $\eta_k \approx 170 \mu m$ at the

321 nozzle lip. The largest value of the ratio $\Delta x / \eta_k$ is thus about $\Delta x / \eta_k \approx 1.35$ at the lip, which is

322 within the range recommended by Pope [59]. It should be noted that the DNS simulation results

323 have been compared against the experimental data of Gounder et al. [14] at different axial

324 distances from the nozzle [23]. Good agreement has been found between the experimental and

325 computational results, and the interested readers are referred to [23,39] for a detailed discussion

326 of these results which will not be repeated here for the sake of brevity.

327

328 **3. RESULTS & DISCUSSION**

329 **3.1 Flame behaviour**

330 Figure 3a shows the instantaneous iso-surface of reaction progress variable $c = 0.8$ coloured

331 with temperature T. It is evident from Fig. 3a that significant wrinkling of the jet flame occurs

332 due to flame-turbulence and flame-droplet interactions. Furthermore, the variations in

333 temperature are indicative of the changes in burning rates due to the variations in equivalence

334 ratio caused by droplet evaporation. The instantaneous fields on the central x-y plane of

335 temperature T, reaction progress variable c, fuel mass fraction $Y_{C_2H_5OH}$, oxygen mass fraction

336 Y_{O_2}, and mixture fraction ξ are shown in Figs. 3b, c, d, e and f, respectively, along with green

337 lines indicating the stoichiometric mixture fraction $\xi_{st} = 0.0914$. Figures 3b-f further

demonstrate the large amounts of wrinkling of the jet flame, which is particularly evident further downstream of the jet exit (i.e. from $x/D_j \approx 5$ onwards). Figure 3b shows the injection of cold gaseous fuel in the inner jet whilst the temperature T increases as the inner jet mixes with the pilot stream, and droplet evaporation can be observed. The droplet evaporation happens relatively quickly for the small droplets, with small regions of gaseous fuel-rich mixture visible close to the jet exit (e.g. $x/D_j \approx 2$), as shown in Figs. 3d and 3f.
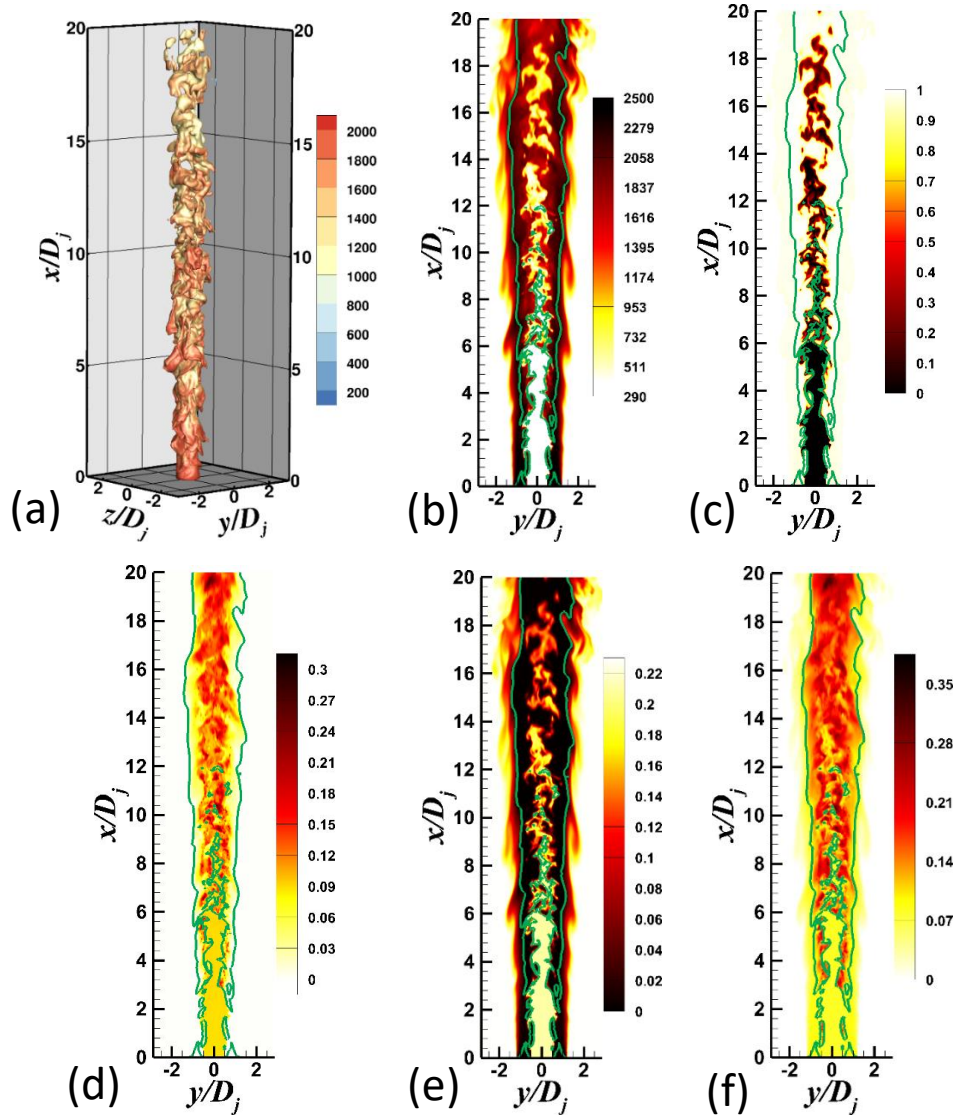
Fig. 3: Instantaneous plots of (a) reaction progress variable $c = 0.8$ iso-surface coloured with temperature T [K], (b) temperature T [K] on the central x-y plane, (c) reaction progress variable c, (d) Ethanol C_2H_6O mass fraction on the central x-y plane, (e) oxygen O_2 mass fraction at the central x-y plane, and (f) mixture fraction ξ at the central x-y plane. In (b)-(f) the green lines indicate the stoichiometric mixture fraction $\xi_{st} = 0.0914$ contours.
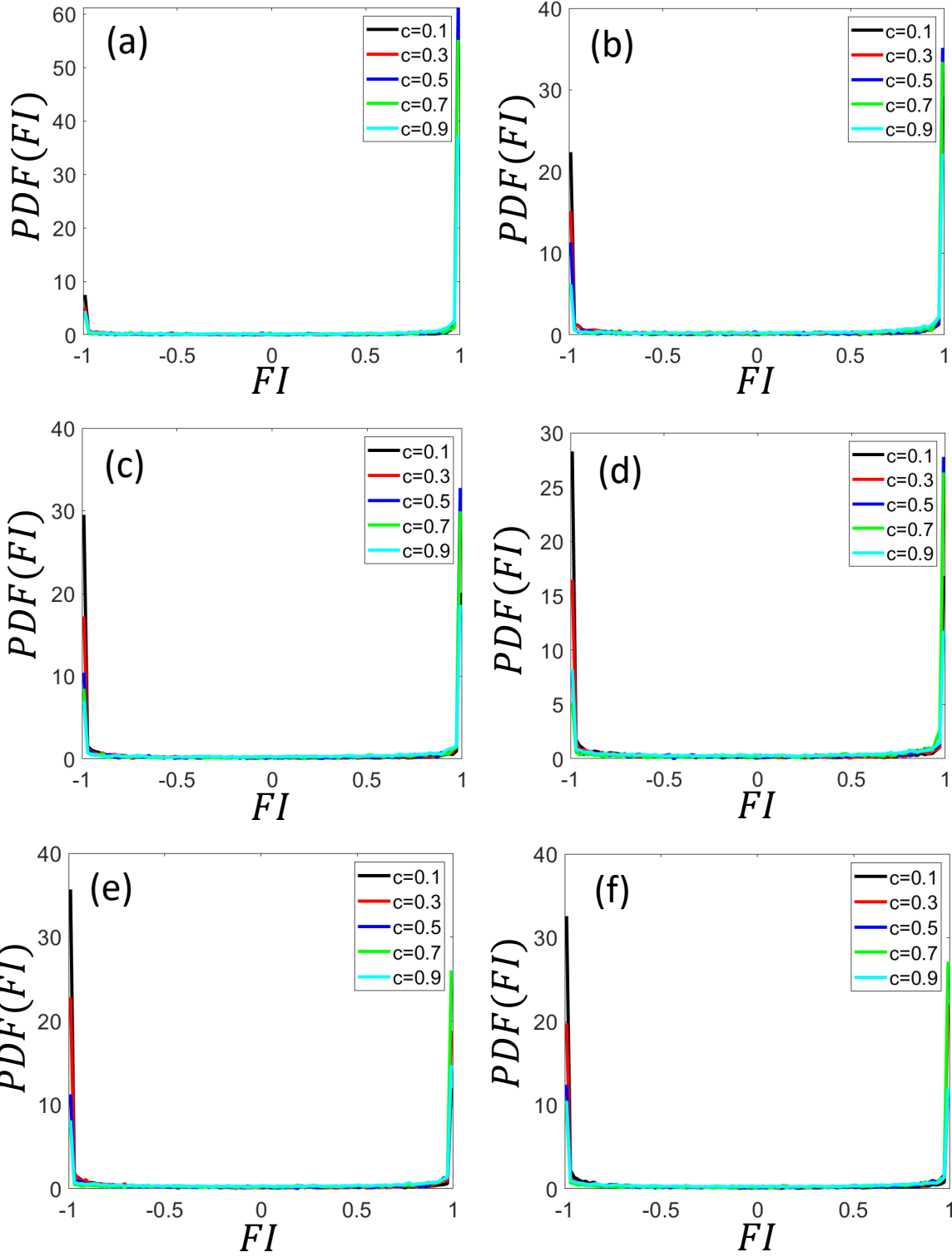
Fig. 4: Probability density functions of Flame Index (i.e. $FI = \nabla Y_{C_2H_6O} \cdot \nabla Y_{O_2} / [|\nabla Y_{C_2H_6O}||\nabla Y_{O_2}|]$) for $c = 0.1, 0.3, 0.5, 0.7$ and 0.9, at (a) $x = 2D_j$, (b) $x = 4D_j$, (c) $x = 6D_j$, (d) $x = 8D_j$, (e) $x = 10D_j$, and (f) $x = 12D_j$.
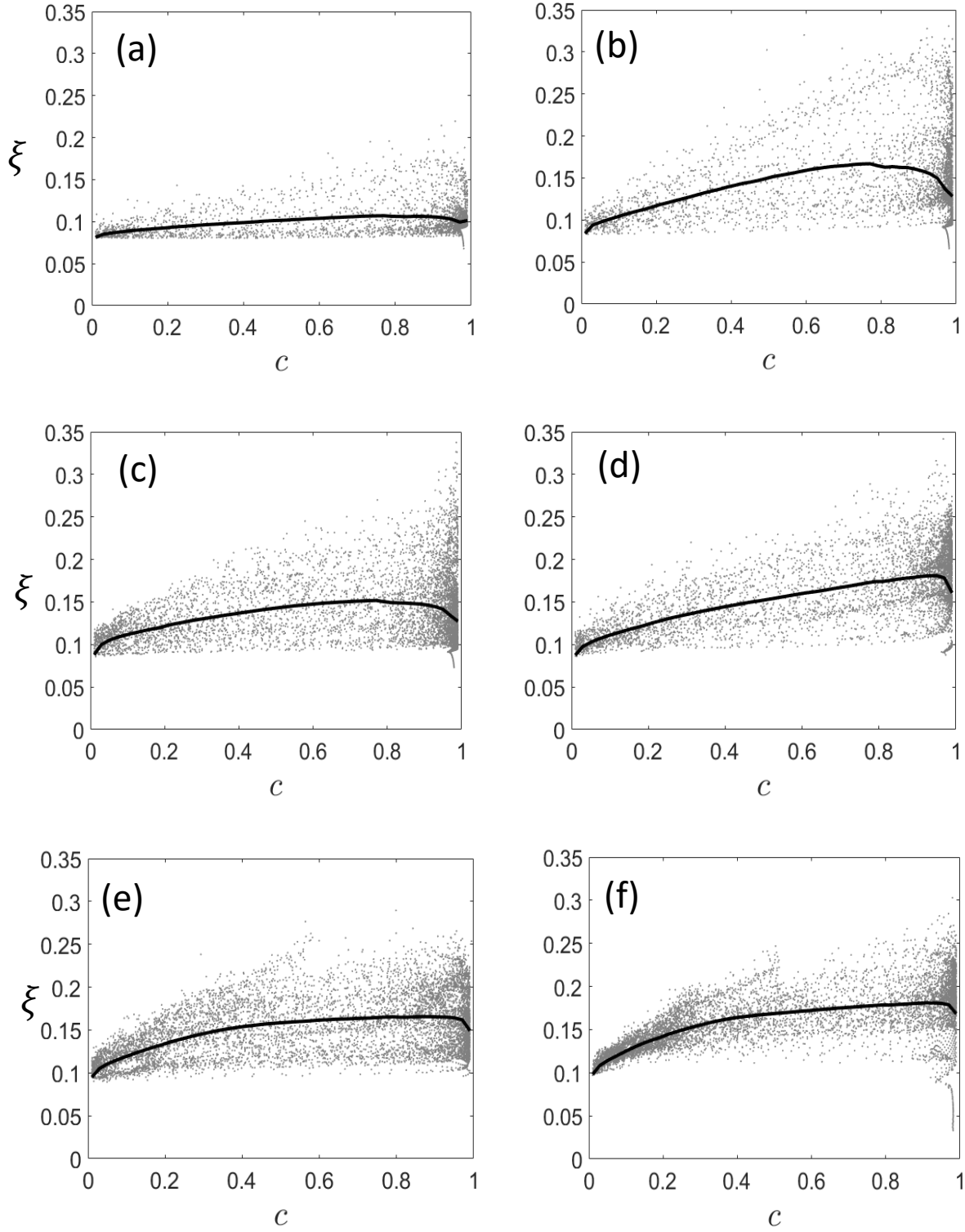
16

362

363

364

Fig. 5: Scatter of mixture fraction ξ (grey dots) with reaction progress variable c and variations of the mean value of mixture fraction ξ conditioned upon c (black line) at (a) $x = 2D_j$, (b) $x = 4D_j$, (c) $x = 6D_j$, (d) $x = 8D_j$, (e) $x = 10D_j$, and (f) $x = 12D_j$.

Further downstream, large droplets also evaporate and give rise to larger hot regions of gaseous fuel-rich mixtures at approximately $x/D_j \approx 5$, as shown in Figs. 3d and 3f. The largest droplets

17

371   do not evaporate until far downstream of the jet exit and the evidence of evaporation can be

372   observed as far as $x/D_j \approx 20$, which is not shown here. The evaporation process occurring in

373   the mixing layer is visible in Fig. 3f in the mixture ξ field, which increases continuously from

374   the nozzle lip and shows large values of ξ/ξ_{st} up to $\xi/\xi_{st} = 2.0$ at $x/D_j = 15$ and $\xi/\xi_{st} = 2.5$

375   at $x/D_j = 20$ before decreasing slowly due to mixing. Further downstream (i.e. $x/D_j > 10$),

376   around the pockets of very high fuel content created by the droplet evaporation, as shown in

377   Figs. 3d and 3f, the burning occurs increasingly in a non-premixed mode because the hot fuel

378   does not have the time to fully mix with the surrounding air leading to partial-premixing, which

379   is characteristic of spray flames. In addition, an animation has been provided in the

380   supplementary material to accompany this paper which shows the mid-plane of the jet coloured

381   with temperature with the spray particles on that plane coloured by the evaporation rate. The

382   nature of the combustion (e.g. premixed, non-premixed) can be characterised by considering a

383   Flame Index, FI, defined as $FI = \nabla Y_{C_2H_6O} \cdot \nabla Y_{O_2} / \left[\left| \nabla Y_{C_2H_6O} \right| \left| \nabla Y_{O_2} \right| \right]$ [60]. A Flame Index value

384   of $FI = -1.0$ indicates non-premixed mode of combustion, whereas a Flame Index value of

385    $FI = 1.0$ indicates premixed mode of combustion. The PDFs of Flame Index at different

386   isosurfaces of the reaction progress variable (i.e. $c = 0.1, 0.3, 0.5, 0.7$ and 0.9) at $x/D_j = 2$,

387   4, 6, 8, 10 and 12 are shown in Figs. 4a-f, respectively. It can be seen from Fig. 4 that close to

388   the nozzle exit (e.g. $x/D_j = 2$) the premixed mode of combustion remains dominant across the

389   flame. However, moving further downstream (i.e. $x/D_j = 4,6,8,10,12$) greater contributions

390   of non-premixed mode of combustion can be seen towards the unburned gas side of the flame

391   (i.e. $c = 0.1$) due to the greater number of droplets beginning to evaporate downstream. The

392   non-premixed mode of combustion decreases (i.e. the PDF peak at $FI = -1.0$ decreases) with

393   increasing c, as mixing progressively takes place within the flame. This supports the

394   observations made earlier in Figs. 3d and 3f.

395

396   The scatters of mixture faction ξ with c as well as the conditional average at $x/D_j = 2, 4, 6$,

397   8, 10 and 12 are shown in Figs. 5a-f, respectively. In the current and subsequent sections, the

398   mean values conditional upon c are determined by considering the ensemble averaged value of

399   the quantity being considered on a given c-isosurface. It is evident from Figs. 5a-f that close to

400   the jet exit there are significant fuel-lean contributions (see Fig. 5a) whilst moving further

401   downstream (see Figs. 5b-f) significant fuel-rich contributions are found due to droplet

402   evaporation. These observations are consistent with those found in Figs. 3d and f. It should be

403   noted that if one examines Fig. 2a and b, at the axial locations considered (i.e. $x/D_j = 2, 4, 6$,

404   8, 10 and 12) the Damköhler number would remain low under stochiometric conditions (i.e.

405   ranging from $Da = 0.9$ to 2.5). Therefore, considering Figs. 2a and b alongside combustion of

406   either fuel-lean or fuel-rich mixtures, it is evident that low Damköhler number conditions are

407   prevalent here. These conditions must be considered when investigating the behaviour of the

408   displacement speed S_d and its components, particularly S_{ev} and S_c.

409

410   **3.2 Density-weighted displacement speed S_d^* behaviour**

411   The scatters of density-weighted displacement speed $S_d^*/S_{b(\phi=1)}$ (where $S_{b(\phi=1)}$ is the laminar

412   burning speed of the stoichiometric mixture) with c as well as the conditional average at

413    $x/D_j = 2, 4, 6, 8, 10$ and 12 are shown in Figs. 6a-f, respectively. It is evident from Figs. 6a-

414   f that the density-weighted displacement speed S_d^* exhibits similar qualitative behaviour at all

415   axial locations considered. It can be seen from the scatters in Figs. 6a-f that the density-

416   weighted displacement speed S_d^* can exhibit both positive and negative values across c but is

417   generally positive as shown by the variations of the mean values conditional upon c. Generally,

418   larger positive values towards the unburned gas side falling towards the burned gas side and

419   potentially exhibiting negative conditionally averaged values around $c = 0.9$ at all axial

420   locations considered. A negative value of S_d^* indicates that the flame retreats into the burned

421   gas instead of propagating into the unburned reactants.

422

423   The sign of the displacement speed S_d is same as that of S_d^*, and, therefore, these plots are not

424   shown here for the sake of brevity. A combination of positive mean values of S_d^* towards the

425   unburned gas side and negative mean values on the burned gas side suggests thickening of the

426   flame, and instances of local flame thickening can be discerned from Fig. 3b. The observed

427   behaviour here is consistent with observations previously made for low Damköhler number

428   premixed and stratified gaseous flames [55]. The observed qualitative and quantitative

429   behaviours of the displacement speed S_d and density-weighted displacement speed S_d^* at

430   different axial locations can be explained in terms of the contributions of $\vec{N} \cdot \nabla(\rho D \vec{N} \cdot \nabla c)$,

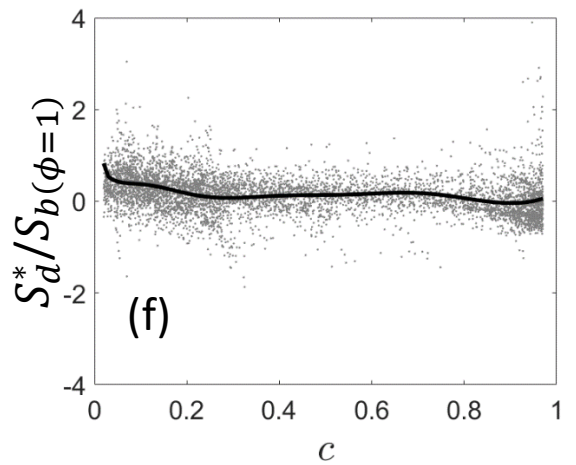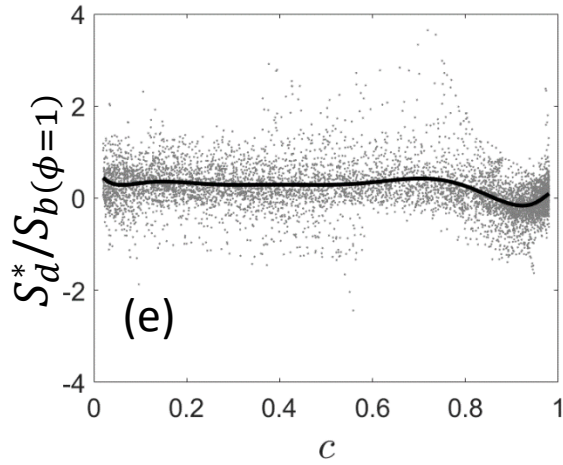431 $(-2\rho D \kappa_m |\nabla c|)$, $\dot{\omega}_c$, $\dot{S}_{ev}$ and $\dot{S}_c$.
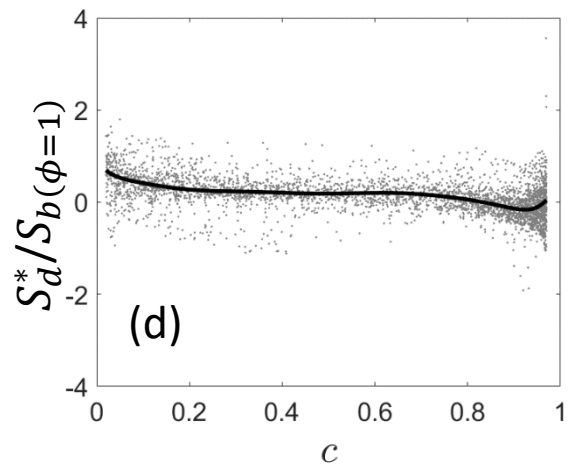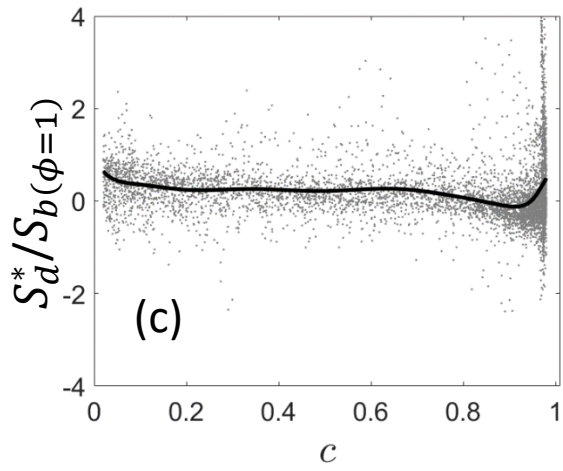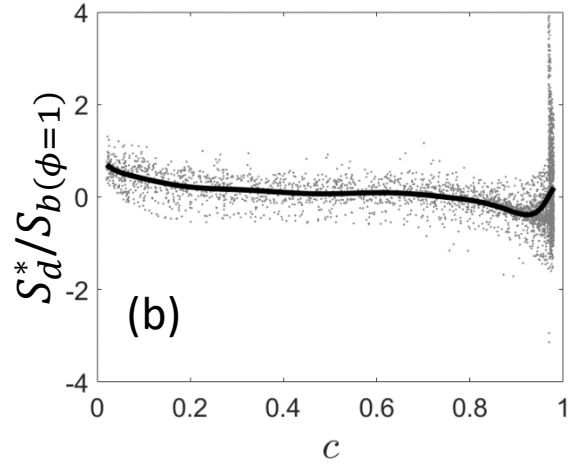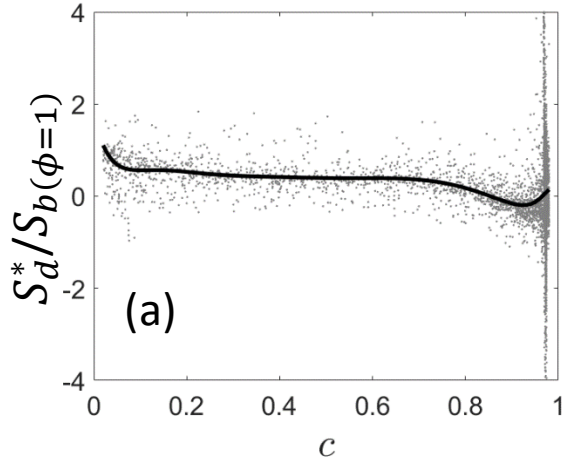
432

19

433

434

435

Fig. 6: Scatter of the variations of density-weighted displacement speed S_d^* (grey dots) with reaction progress variable c and mean values of density-weighted displacement speed conditioned upon c (black line) at (a) $x = 2D_j$, (b) $x = 4D_j$, (c) $x = 6D_j$, (d) $x = 8D_j$, (e) $x = 10D_j$, and (f) $x = 12D_j$. All quantities are normalised by normalised using the unstrained laminar burning velocity of the stoichiometric mixture $S_{b(\phi=1)}$.
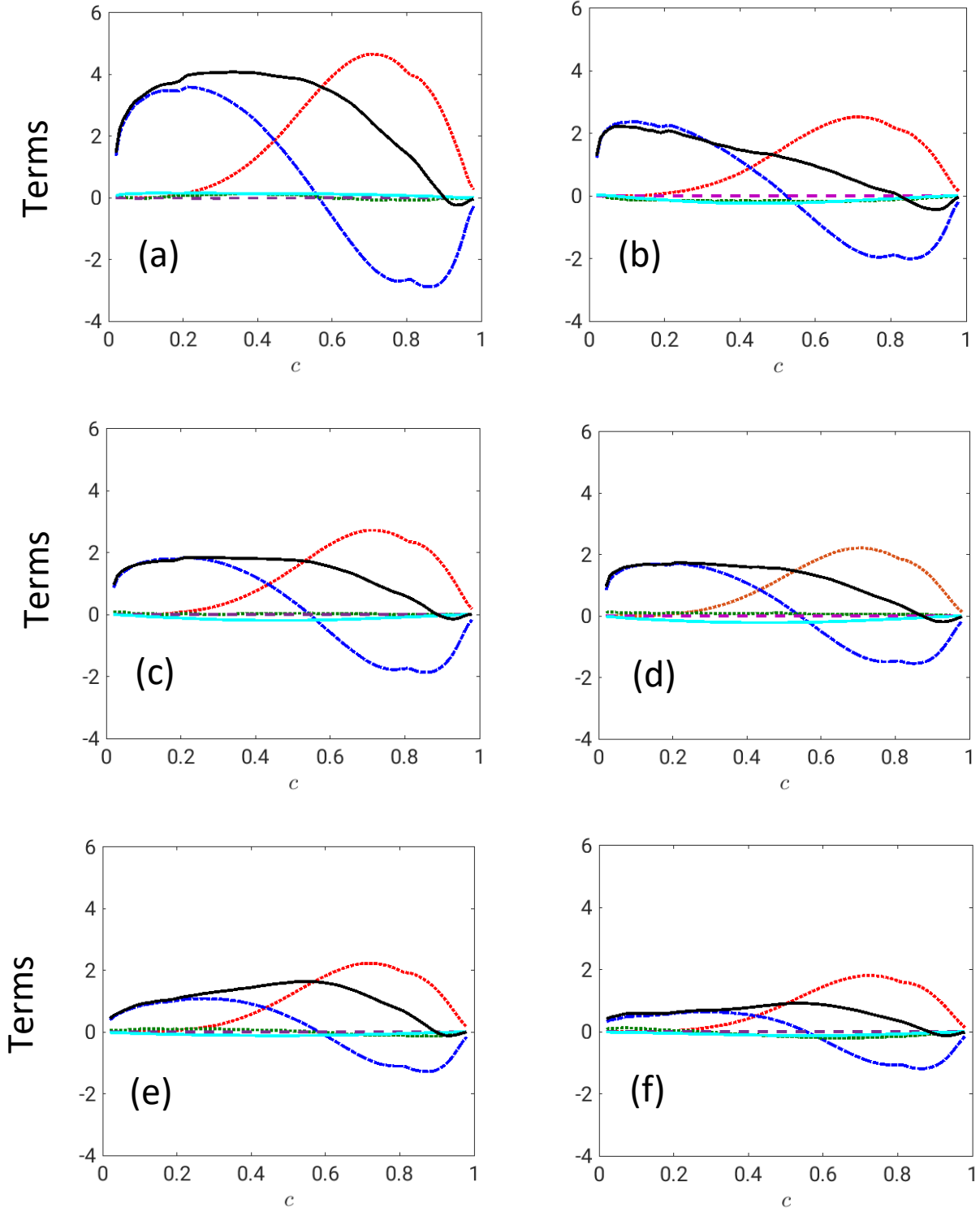
441

442

443

Fig. 7: Variations of the mean values of $\vec{N} \cdot \nabla(\rho D \vec{N} \cdot \nabla c)$ [---], $(-2\rho D \kappa_m |\nabla c|)$ [.....], $\dot{\omega}_c$ [.....], $\dot{S}_{ev}$ [--] and $\dot{S}_c$ [——] as well as the combined contribution of the contributions [——] conditioned upon reaction progress variable c at (a) $x = 2D_j$, (b) $x = 4D_j$, (c) $x = 6D_j$, (d) $x = 8D_j$, (e) $x = 10D_j$, and (f) $x = 12D_j$. All quantities are normalised using $\rho_0 S_{b(\phi=1)} / \delta_{th(\phi=1)}$ where $\delta_{th(\phi=1)}$ and $S_{b(\phi=1)}$ are the thermal flame thickness and unstrained laminar burning velocity of the stoichiometric mixture, respectively.
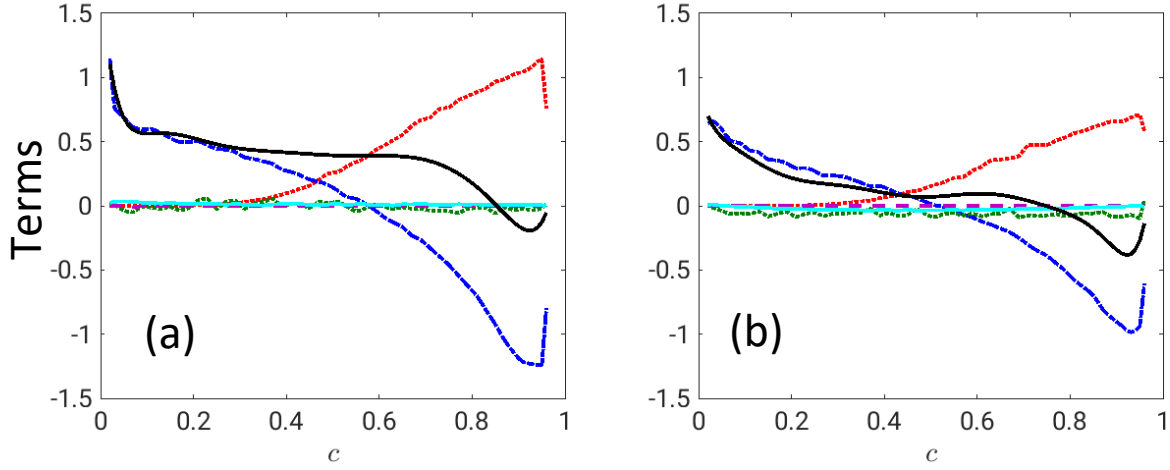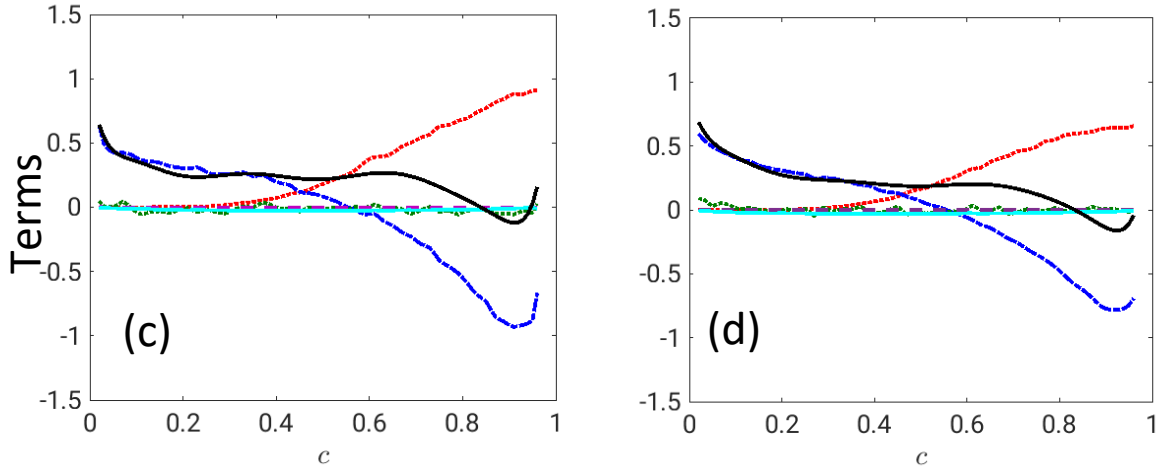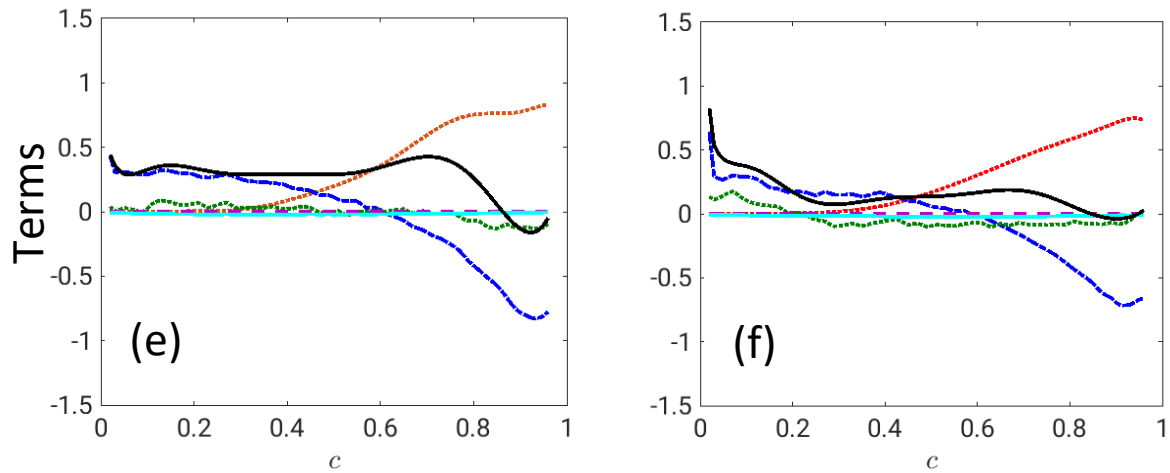
Fig. 8: Variations of the mean values of density-weighted displacement speed S_d^* [——] and its components (i.e. S_r^* [······], S_n^* [– – –], S_t^* [······], S_{ev}^* [– –] and S_c^* [——]) conditioned upon reaction progress variable c at (a) $x = 2D_j$, (b) $x = 4D_j$, (a) $x = 6D_j$, (a) $x = 8D_j$, (a) $x = 10D_j$, and (a) $x = 12D_j$. All quantities are normalised using $S_{b(\phi=1)}$.

460 The variations of the mean values of $\dot{\omega}_c$, $\vec{N} \cdot \nabla(\rho D \vec{N} \cdot \nabla c)$, $(-2\rho D \kappa_m |\nabla c|)$, $\dot{S}_{ev}$ and $\dot{S}_c$

461 (normalised by $\rho_0 S_{b(\phi=1)}/\delta_{th(\phi=1)}$ where $\delta_{th(\phi=1)}$ is the thermal flame thickness of the

462 laminar stoichiometric mixture) conditional upon c as well as their combined contributions are

463 shown for $x/D_j = 2, 4, 6, 8, 10$ and 12 in Figs. 7a-f, respectively. It is evident from Figs. 7a-

464 f that the mean value of reaction rate of reaction progress variable $\dot{\omega}_c$ is deterministically

465 positive across c at all axial locations considered here exhibiting similar qualitative behaviour

466 - small values towards the unburned gas side with larger values towards the burned gas side

467 and a peak value close to $c = 0.7$ in the reaction zone. The magnitude of the mean values of

468 $\dot{\omega}_c$ has been found to decrease moving downstream of the jet exit which is due to the

469 evaporation of larger droplets leading to fuel-rich conditions and thus giving rise to reduced

470 burning rates. Furthermore, $\dot{\omega}_c$ acts as a leading order term for all axial locations considered

471 here. The mean flame normal molecular diffusion contribution $\vec{N} \cdot \nabla(\rho D \vec{N} \cdot \nabla c)$ shows similar

472 qualitative behaviour at all axial locations considered – exhibiting positive mean values

473 towards the unburned gas side and negative mean values towards the burned gas side with a

474 transition close to $c = 0.55$. The magnitudes of the mean values of $\vec{N} \cdot \nabla(\rho D \vec{N} \cdot \nabla c)$

475 conditional upon c have been found to decrease moving downstream of the jet exit as a result

476 of increased flame thickness for fuel-rich mixtures. However, $\vec{N} \cdot \nabla(\rho D \vec{N} \cdot \nabla c)$ acts as a

477 leading order term for all axial locations considered here. The mean tangential molecular

478 diffusion $(-2\rho D \kappa_m |\nabla c|)$ conditional upon c has been found to be small in comparison to the

479 mean values of $\dot{\omega}_c$ and $\vec{N} \cdot \nabla(\rho D \vec{N} \cdot \nabla c)$ at all axial locations considered in the current analysis.

480 The mean value of the term arising due to droplet evaporation $\dot{S}_{ev}$ has been shown to be

481 negligible across c for all axial locations considered in the current analysis. The mean value of

482 the cross-scalar dissipation contribution $\dot{S}_c$ has been shown to be small, but non-negligible,

483 across c for all axial locations considered. It should be noted that the mean contribution of $\dot{S}_c$

484 exhibits positive values across c at $x/D_j = 2$. However, at axial locations further

485 downstream, $\dot{S}_c$ exhibits negative mean values. It is evident, therefore, that the combined

486 contribution of $\dot{\omega}_c$, $\vec{N} \cdot \nabla(\rho D \vec{N} \cdot \nabla c)$, $(-2\rho D \kappa_m |\nabla c|)$, $\dot{S}_{ev}$ and $\dot{S}_c$ is predominantly determined

487 by the competition between the contributions of $\dot{\omega}_c$ and $\vec{N} \cdot \nabla(\rho D \vec{N} \cdot \nabla c)$. The observations

488 made here are consistent with those previously made for the mean variations of $\dot{\omega}_c$, $\vec{N} \cdot$

489 $\nabla(\rho D \vec{N} \cdot \nabla c)$, $(-2\rho D \kappa_m |\nabla c|)$, $\dot{S}_{ev}$ and $\dot{S}_c$ conditional upon c for turbulent spray flames in

490 canonical configurations [20,27]. It can be seen from Figs. 7a-f that the mean value of the

491 combined contribution of $\dot{\omega}_c$, $\vec{N} \cdot \nabla(\rho D \vec{N} \cdot \nabla c)$, $(-2\rho D \kappa_m |\nabla c|)$, $\dot{S}_{ev}$ and $\dot{S}_c$ remains positive

492 for the majority of the flame but small negative values are obtained towards the burned gas

493 side, as the negative contribution of $\vec{N} \cdot \nabla(\rho D \vec{N} \cdot \nabla c)$ overcomes the positive contributions.

494 The variations of the mean values of the density-weighted displacement speed S_d^* and its

495 contributions S_r^*, S_n^*, S_t^*, S_{ev}^* and S_c^* conditional upon c are shown for $x/D_j = 2, 4, 6, 8, 10$

496 and 12 in Figs. 8a-f, respectively. It can be seen from Figs. 8a-f that the general behaviours of

497 the contributions of S_r^*, S_n^*, S_t^*, S_{ev}^* and S_c^* are consistent with behaviours of $\dot{\omega}_c$, $\vec{N} \cdot$

498 $\nabla(\rho D \vec{N} \cdot \nabla c)$, $(-2\rho D \kappa_m |\nabla c|)$, $\dot{S}_{ev}$ and $\dot{S}_c$. Furthermore, the observed behaviour for the mean

499 value of the combined contributions of $\dot{\omega}_c$, $\vec{N} \cdot \nabla(\rho D \vec{N} \cdot \nabla c)$, $(-2\rho D \kappa_m |\nabla c|)$, $\dot{S}_{ev}$ and $\dot{S}_c$ is

500 consistent with the general behaviour observed for the mean values of density-weighted

501 displacement speed S_d^*. Accordingly, the behaviour of the density-weighted displacement

502 speed S_d^* is predominantly determined by the competition between the reaction rate component

503 S_r^* and the normal molecular diffusion component S_n^*. Moreover, the mean contributions of S_t^*,

504 S_{ev}^* and S_c^* remain small in magnitude in comparison to the leading order contributions of S_r^*

505 and S_n^*. These observations are, again, consistent with those previously made for turbulent

506 spray flames in canonical configurations [20,27].

507 It should be noted that, from a modelling perspective, it is often useful to know the curvature

508 (i.e. $\kappa_m = \nabla \cdot \vec{N}/2$) and tangential strain rate (i.e. $a_T = (\delta_{ij} - N_i N_j)(\partial u_i/\partial x_j)|_{c=c^*}$) dependencies

509 of the density-weighted displacement speed S_d^* and its components. Table 3 shows the

510 correlation coefficients for $\kappa_m - a_T$, $\kappa_m - S_d^*$, $\kappa_m - S_r^*$, $\kappa_m - S_n^*$, $\kappa_m - S_t^*$, $a_T - S_d^*$, $a_T - S_r^*$,

511 $a_T - S_n^*$ and $a_T - S_t^*$ at $c = 0.7$ (i.e. the location within the flame of the maximum reaction

512 rate) for all axial locations considered in the current study (i.e. $x/D_j = 2, 4, 6, 8, 10$ and 12).

513 It can be seen from Table 3 that $\kappa_m - a_T$ exhibits weak negative correlations at all axial

514 locations considered but that the extent of the negative correlation is generally larger moving

515 further downstream. These general observations are consistent with previous findings in

516 turbulent stratified flames under canonical configurations [55] and turbulent premixed jet

517 flames [61].

518

519

520

521

Table 3: Correlation coefficients of $\kappa_m - a_T$, $\kappa_m - S_d^*$ $\kappa_m - S_r^*$, $\kappa_m - S_n^*$, $\kappa_m - S_t^*$, $a_T - S_d^*$, $a_T - S_r^*$,

$a_T - S_n^*$ and $a_T - S_t^*$ across the jet at $x/D_j = 2, 4, 6, 8, 10$ and 12 for $c = 0.7$ isosurface

x/D_j	2	4	6	8	10	12
$\kappa_m - a_T$	-0.2063	-0.0673	-0.4344	-0.2533	-0.2060	-0.3291
$\kappa_m - S_d^*$	-0.7387	-0.6670	-0.7892	-0.7598	-0.7787	-0.6699
$\kappa_m - S_r^*$	-0.0426	0.2227	0.0147	0.3181	-0.3665	0.1866
$\kappa_m - S_n^*$	-0.0065	0.0326	-0.2670	-0.2359	-0.3388	-0.0830
$\kappa_m - (S_r^* + S_n^*)$	-0.0342	0.2366	-0.1305	0.1752	-0.4236	0.1083
$\kappa_m - S_t^*$	-0.9983	-0.9861	-0.9943	-0.9962	-0.9963	-0.9971
$a_T - S_d^*$	-0.0120	-0.1784	0.2709	-0.0015	0.0563	-0.0416
$a_T - S_r^*$	-0.2310	-0.0820	0.0781	-0.2036	-0.0319	-0.3804
$a_T - S_n^*$	-0.1941	-0.4994	-0.1958	-0.2972	-0.1358	-0.2017
$a_T - (S_r^* + S_n^*)$	-0.2727	-0.2840	-0.0422	-0.3379	-0.0703	-0.3917
$a_T - S_t^*$	0.2023	0.0481	0.4128	0.2624	0.2224	0.3331

It is well-known that S_d^* in turbulent premixed and stratified flames exhibits considerable strain rate and curvature dependences [55-57], and a qualitatively similar behaviour has been reported for turbulent spray flames in canonical configurations. Therefore, it is worthwhile to examine the curvature and strain rate dependences of S_d^* in the configuration considered here. The correlation coefficients for S_d^* and its leading order components with local tangential strain rate a_T and curvature κ_m at different axial locations are exemplarily shown for $c = 0.7$ isosurface in Table 3. The mean value of reaction rate $\dot{\omega}_c$ assumes its peak value close to $c = 0.7$ and thus the $c = 0.7$ isosurface can be taken to represent the flame surface for the following discussion in accordance with previous analyses [55-57]. It can be seen from Table 3 that S_d^* exhibits negative correlation with curvature κ_m at all axial locations considered. This negative correlation is consistent with previous findings in turbulent premixed and stratified flames [55-57]. To better understand the behaviour of the $\kappa_m - S_d^*$ correlation, it is necessary to examine the curvature dependence of the leading components of the density-weighted displacement speed. It is evident from Table 3 that S_r^* and κ_m are generally weakly, but predominantly positively, correlated whereas S_n^* shows weak, but predominantly negative, correlation with κ_m (both observations being consistent with previous studies on turbulent premixed and

541   stratified flames [55-57]). Table 3 also shows a weak correlation between κ_m and $(S_r^* + S_n^*)$

542   (i.e. the two major contributors to S_d^*). However, S_t^* and κ_m are found to be (deterministically)

543   negatively correlated, as the mass diffusivity D on a given c isosurface is not expected to

544   exhibit any appreciable correlation with κ_m. This strong negative $\kappa_m - S_t^*$ correlation is

545   principally responsible for the negative correlation between S_d^* and κ_m, which is consistent

546   with previous findings based on turbulent premixed and stratified flames [55-57].

547   Table 3 shows that a_T and S_d^* exhibit weak correlations for all axial locations considered here,

548   which is consistent with previous analyses on turbulent premixed and stratified flames [55-57].

549   To better understand the behaviour of the correlation between a_T and S_d^*, it is useful to examine

550   the tangential strain rate dependencies of the leading components of the density-weighted

551   displacement speed. It is evident from Table 3 that a_T and S_r^* are weakly and predominantly

552   negatively correlated, and that a_T and S_n^* are negatively correlated at all axial locations

553   considered in the current study (both observations are consistent with previous analyses on

554   turbulent premixed and stratified flames [55-57]). Table 3 also shows that the correlation

555   between a_T and $(S_r^* + S_n^*)$ (i.e. the two major contributors to S_d^*) is weakly negatively

556   correlated at all axial locations considered and this negative correlation is consistent with

557   previous analyses on turbulent premixed and stratified flames [55-57]. As the mean curvature

558   and tangential strain rate are negatively correlated, the tangential component of displacement

559   speed $S_t = -2D\kappa_m$ and a_T are expected to be positively correlated in all cases which can be

560   verified from weak positive $a_T - S_t^*$ correlation in Table 3 at all axial locations considered

561   here. This has been found to be consistent with previous studies on turbulent premixed and

562   stratified flames [55-57]. The positive $a_T - S_t^*$ correlation overcomes the negative correlation

563   between a_T and $(S_r^* + S_n^*)$ to gives rise to a weak correlation between a_T and S_d^* (see Table

564   3). It is worth noting that the statistics of S_d^*, and its local curvature and tangential strain rate

565   dependences for the jet flame considered here are also found to be qualitatively similar to the

566   spray flames in canonical configurations (e.g. statistically planar or spherical flames) [20,26].

567   The physical explanations for the observed curvature and tangential strain rate dependences of

568   S_d^* components have been provided elsewhere [20,26,55-57] in detail and thus will not be

569   repeated here.

570

571   **3.3 Implications and further considerations**

572   The statistical behaviours of the mean contributions of $\dot{\omega}_c$, $\vec{N} \cdot \nabla(\rho D \vec{N} \cdot \nabla c)$, $(-2\rho D \kappa_m |\nabla c|)$,

573    $\dot{S}_{ev}$ and $\dot{S}_c$ offer useful insights into the modelling aspects for turbulent spray flames. Firstly,

574 it should be noted that the qualitative nature of the mean variations of $\dot{\omega}_c$, $\vec{N} \cdot \nabla(\rho D \vec{N} \cdot \nabla c)$,

575 $(-2\rho D \kappa_m |\nabla c|)$, $\dot{S}_{ev}$ and $\dot{S}_c$ observed here is consistent with those observed in turbulent spray

576 flames for canonical configurations [20,27], which suggests that the flow geometry in the

577 absence of mean flame curvature might not be an important factor in the behaviour of these

578 terms. Moreover, the observed mean behaviours of $\dot{\omega}_c$, $\vec{N} \cdot \nabla(\rho D \vec{N} \cdot \nabla c)$, $(-2\rho D \kappa_m |\nabla c|)$ and

579 $\dot{S}_c$ are consistent with observations made for these quantities in turbulent stratified gaseous

580 flames [55]. This suggests that the same modelling methodologies that have been employed

581 with respect to turbulent stratified flames might be possible to extend for turbulent spray

582 flames.

583 In the context of the FSD modelling approach [28,61,62], the following assumption is often

584 invoked:

585 $$\rho S_d |\nabla c| = \dot{\omega}_c + \vec{N} \cdot \nabla(\rho D \vec{N} \cdot \nabla c) - 2\rho D \kappa_m |\nabla c| + \dot{S}_{ev} + \dot{S}_c \approx \rho_0 S_{b(\phi)} |\nabla c| \qquad (45)$$

586 where ρ_0 is the unburned reactant density and $S_{b(\phi)}$ is the laminar burning speed as a function

587 of the local equivalence ratio ϕ. The variations of the mean values of $\rho_0 S_{b(\phi)} |\nabla c|$ and the

588 combined contribution of $\dot{\omega}_c + \vec{N} \cdot \nabla(\rho D \vec{N} \cdot \nabla c) - 2\rho D \kappa_m |\nabla c| + \dot{S}_{ev} + \dot{S}_c$ conditional upon c

589 are shown in Figs. 9a-f for $x/D_j = 2, 4, 6, 8, 10$ and 12. It can be seen from Figs. 9a-f that the

590 approximation of $\dot{\omega}_c + \vec{N} \cdot \nabla(\rho D \vec{N} \cdot \nabla c) - 2\rho D \kappa_m |\nabla c| + \dot{S}_{ev} + \dot{S}_c$ using $\rho_0 S_{b(\phi)} |\nabla c|$

591 provides poor agreement across c for all axial locations considered in the current study. It is

592 evident that the mean values of $\rho_0 S_{b(\phi)} |\nabla c|$ largely overpredict the mean values of $\dot{\omega}_c + \vec{N} \cdot$

593 $\nabla(\rho D \vec{N} \cdot \nabla c) - 2\rho D \kappa_m |\nabla c| + \dot{S}_{ev} + \dot{S}_c$ for axial locations $x/D_j = 2, 4, 6, 8$. This finding is

594 consistent with previous analyses of low Damköhler number turbulent premixed and stratified

595 gaseous flames [55]. Whilst the extent of over-prediction is relatively small at $x/D_j = 10$ and

596 12, the qualitative trends of $\dot{\omega}_c + \vec{N} \cdot \nabla(\rho D \vec{N} \cdot \nabla c) - 2\rho D \kappa_m |\nabla c| + \dot{S}_{ev} + \dot{S}_c$ are not captured

597 by $\rho_0 S_{b(\phi)} |\nabla c|$. Furthermore, it should be noted $\dot{\omega}_c + \vec{N} \cdot \nabla(\rho D \vec{N} \cdot \nabla c) - 2\rho D \kappa_m |\nabla c| + \dot{S}_{ev} +$

598 $\dot{S}_c$ exhibits negative values which $\rho_0 S_{b(\phi)} |\nabla c|$ cannot adequately account for. On Reynolds

599 averaging/LES filtering Eq. 45 one obtains: $\overline{(\rho S_d)}_s = \rho_0 S_{b(\phi)}$ (where $\overline{(Q)}_s = \overline{Q|\nabla c|}/\overline{|\nabla c|}$ is

600 the surface-weighted value of a general quantity Q [61,62]), which is often used for the FSD

601 based closures in turbulent premixed and stratified flames [62-64]. However, the inequality of

602 left- and right-hand sides of Eq. 45 reveals that such modelling approaches might not be

603 appropriate for low Damköhler number spray flames in general and that alternative modelling
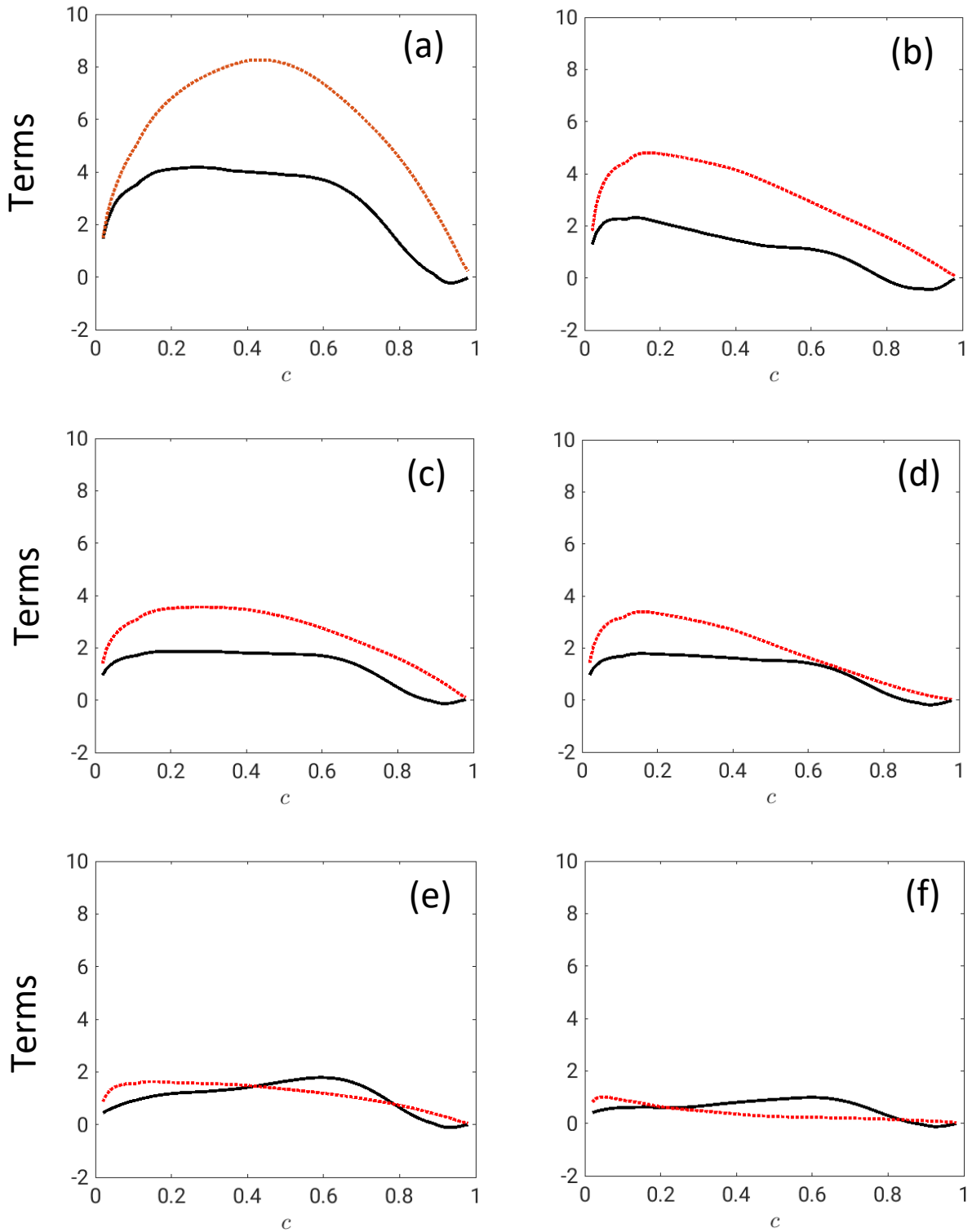604 approaches might need to be considered.

605

606

607

608 **Fig. 9:** Variations of the mean values of $\dot{\omega}_c + \vec{N} \cdot \nabla(\rho D \vec{N} \cdot \nabla c) - 2\rho D \kappa_m |\nabla c| + \dot{S}_{ev} + \dot{S}_c$ [
609 ———] and $\rho_0 S_{b(\phi)} |\nabla c|$ [·······] conditioned upon reaction progress variable c at (a)
610 $x = 2D_j$, (b) $x = 4D_j$, (c) $x = 6D_j$, (d) $x = 8D_j$, (e) $x = 10D_j$, and (f) $x = 12D_j$. All
611 quantities are normalised using $\rho_0 S_{b(\phi=1)} / \delta_{th(\phi=1)}$.

4. CONCLUSIONS

In the current study, a three-dimensional Direct Numerical Simulation of an open turbulent jet spray flame representing a laboratory-scale burner configuration [14] has been considered to investigate the behaviour of the density-weighted displacement speed S_d^* and its components. The open turbulent jet spray flame has been found to exhibit fuel-lean conditions close to the jet exit, but fuel-rich conditions have been observed further downstream due to the evaporation of fuel droplets. It has been found that the displacement speed S_d and density-weighted displacement speed S_d^* show qualitatively similar behaviour for all axial locations considered – predominantly positive mean values across the flame but with small, potentially negative, mean values towards the burned gas side. It is also found that the observed mean behaviours of the displacement speed and density-weighted displacement speed are fundamentally determined by the contributions of $\dot{\omega}_c$, $\vec{N} \cdot \nabla(\rho D \vec{N} \cdot \nabla c)$, $(-2\rho D \kappa_m |\nabla c|)$, $\dot{S}_{ev}$ and $\dot{S}_c$. The reaction rate $\dot{\omega}_c$ and normal molecular diffusion rate $\vec{N} \cdot \nabla(\rho D \vec{N} \cdot \nabla c)$ are found to be leading order contributors and that the competition between their contributions determines the mean behaviour of the density weighted displacement speed. These observations are consistent with previous studies of turbulent spray flames in a canonical configuration and low Damköhler number turbulent premixed and stratified gaseous flames. This suggests that the flow geometry in the absence of mean curvature might not play an important role in deciding the general behaviour of the displacement speed and its components. This further indicates that the modelling methodologies, which are employed for turbulent stratified flames, might have the potentials to be extended for turbulent spray flames. However, the surface-weighted value of the product of displacement speed with local density cannot be approximated by the product of unburned gas density and the local laminar burning velocity for the sampling locations considered here. This is consistent with previous findings for low Damköhler number stratified flames and thus the modelling methodologies in the context of turbulent spray flames need to account for attributes of low Damköhler number combustion. These aspects will form the basis of future investigations.

REFERENCES

[1] Heywood, J.B. Internal Combustion Engine Fundamentals, 1st edn. McGraw Hills (1998).

[2] Aggarwal, S.K.: A review of spray ignition phenomena: present status and future research. Prog. Energy Combust. Sci. **24**, 565–600 (1998).

[3] Lefebvre, A.H. Gas Turbine Combustion, 2nd edn. Taylor & Francis, Ann Arbor, Michigan, USA (1998).

[4] Bowen, P.: Combustion hazards posed by hybrid fuel systems. Proceedings 5th European Combustion Meeting, Cardiff, UK (2011).

[5] Burgoyne, J.H., Cohen, L.: The effect of drop size on flame propagation in liquid aerosols. Proc. Roy. Soc. Lond. A **225**, 375–392 (1954).

[6] Szekely, Jr., G.A., Faeth, G.M.: Effects of envelope flames on drop gasification rates in turbulent diffusion flames. Combust. Flame **49**, 255–259 (1983).

[7] Faeth, G.M.: Mixing, transport and combustion sprays. Prog. Energy Combust. Sci. **13**, 293–345 (1987).

[8] Ballal, D.R., Lefebvre, A.H.: Flame propagation in heterogeneous mixtures of fuel droplets, fuel vapour and air. Proc. Combust. Inst. **18**, 312–328 (1981).

[9] Hayashi, S., Kumagai, S., Sakai, T.: Propagation velocity and structure of flames in droplet-vapor-air mixtures. Combust. Sci. Technol. **15**, 169–177 (1976).

[10] Silverman, I., Greenberg, J.B., Tambour, Y.: Stoichiometry and polydisperse effects in premixed spray flames. Combust. Flame **93**, 97–118 (1993).

[11] Nomura, H., Koyama, M., Miyamoto, H., Ujiie, Y., Sato, J., Kono, M., Yoda, S.: Microgravity experiments of flame propagation in ethanol droplet-vapor-air mixture. Proc. Combust. Inst. **28**, 999–1005 (2000).

[12] Aggarwal, S.K., Sirignano, W.A.: Unsteady spray flame propagation in a closed volume. Combust. Flame **62**, 69–84 (1985).

[13] Lawes, M., Saat, A.: Burning rates of turbulent iso-octane aerosol mixtures in spherical flame explosions. Proc. Combust. Inst. **33**, 2047–2054 (2011).

[14] Gounder JD, Kourmatzis A, Masri AR. Turbulent piloted dilute spray flames: flow fields and droplet dynamics. Combust Flame. **159** (11), 3372–97 (2012).

[15] Nakamura, M., Akamatsu, F., Kurose, R., Katsuki, M.: Combustion mechanism of liquid fuel spray in a gaseous flame. Phys. Fluids **17**, 123301-123314 (2005).

[16] Watanabe, H., Kurose, R., Hwang, S.-M., Akamatsu, F.: Characteristics of flamelets in spray flames formed in a laminar counterflow. Combust. Flame **148**, 234–248 (2007).

[17] Watanabe, H., Kurose, R., Komori, S., Pitsch, H.: Effects of radiation on spray flame characteristics and soot formation. Combust. Flame **152**, 2–13 (2008).

[18] Neophytou, A., Mastorakos, E.: Simulations of laminar flame propagation in droplet mists. Combust. Flame **156**, 1627–1640 (2009).

[19] Fujita, A., Watanabe, H., Kurose, R., Komori, S.: Two-dimensional direct numerical simulation of spray flames – Part 1: Effects of equivalence ratio, fuel droplet size and radiation, and validity of flamelet model. Fuel **104**, 515–525 (2013).

[20] Wacks, D.H., Chakraborty, N., Mastorakos, E.: Statistical analysis of turbulent flame-droplet interaction: A Direct Numerical Simulation Study. Flow Turb. Combust. **96**, 573-607 (2016).

[21] Wacks D.H., Chakraborty N.: Flame structure and propagation in turbulent flame-droplet interaction: a direct numerical simulation analysis. Flow Turb. Combust. **96**, 1053–1081 (2016).

[22] Pillai A.L., Kurose R.: Numerical investigation of combustion noise in an open turbulent spray flame. Appl Acoust., **133**, 16–27(2018).

[23] Pillai A.L., Kurose R.: Combustion noise analysis of a turbulent spray flame using a hybrid DNS/APE-RF approach. Combust Flame **200**, 168–191 (2019).

[24] Ozel Erol, G., Hasslberger, J., Klein, M., Chakraborty, N.: A Direct Numerical Simulation analysis of spherically expanding turbulent flames in fuel droplet-mists for an overall equivalence ratio of unity, Phys. Fluids, **30**, 086104 (2018).

[25] Ozel Erol, G., Hasslberger, J., Klein, M., Chakraborty, N.: A Direct Numerical Simulation investigation of spherically expanding flames propagating in fuel droplet-mists for different droplet diameters and overall equivalence ratios, Combust. Sci. Technol., **191,** 833-867(2019).

[26] Ozel Erol, G., Hasslberger, J., Klein, M., Chakraborty, N.: Propagation of spherically expanding turbulent flames into fuel droplet-mists, Flow Turb. Combust, https://doi.org/10.1007/s10494-019-00035-x, 2019 (2019).

[27] Ozel Erol, G., Hasslberger, J., Chakraborty, N.: Surface density function evolution in spherically expanding flames in globally stoichiometric droplet-laden mixtures, Combust. Sci. Technol., https://doi.org/10.1080/00102202.2019.1678373 (2019).

[28] Candel, S.M., and Poinsot, T.J.: Flame stretch and the balance equation for the flame area, *Combust. Sci. Tech.*, **70**,1-15 (1990).

713 [29] Peters, N., Turbulent Combustion, *Cambridge Monograph on Mechanics*, Cambridge
714 University Press, Cambridge (2000).

715 [30] Proch, F., Domingo, P., Vervisch, L., Kempf, A. M.: Flame resolved simulation of a
716 turbulent premixed bluff-body burner experiment. Part I: Analysis of the reaction zone
717 dynamics with tabulated chemistry, Combust. Flame **180**, 321-339 (2017).

718 [31] Sandeep, A., Proch, F., Kempf, A.M., Chakraborty, N.: Statistics of strain rates and
719 Surface Density Function in a flame-resolved high-fidelity simulation of a turbulent
720 premixed bluff body burner, Phys. Fluids **30**, 065101(2018).

721 [32] Sankaran, R., Hawkes, E.R., Yoo, C.S., Chen, J.H.: Response of flame thickness and
722 propagation speed under intense turbulence in spatially developing lean premixed
723 methane–air jet flames. Combust. Flame **162**, 3294-3306 (2015).

724 [33] Yu, R., Nillson, T., Bai, X-S., Lipatnikov, A.N.: Evolution of averaged local premixed
725 flame thickness in a turbulent flow. Combust. Flame **207**, 232-249 (2019).

726 [34] Kitano T, Nishio J, Kurose R, Komori S.: Effects of ambient pressure, gas temperature
727 and combustion reaction on droplet evaporation. Combust Flame **161**(2), 551–564
728 (2014).

729 [35] Kitano T, Nishio J, Kurose R, Komori S.: Evaporation and combustion of
730 multicomponent fuel droplets. Fuel **136**, 219–225 (2014).

731 [36] Kurose R, Makino H, Komori S, Nakamura M, Akamatsu F, Katsuki M.: Effects of
732 outflow from the surface of a sphere on drag, shear lift, and scalar diffusion. Phys Fluids
733 **15**(8):2338–2351 (2003).

734 [37] Hara T, Muto M, Kitano T, Kurose R, Komori S.: Direct numerical simulation of a
735 pulverized coal jet flame employing a global volatile matter reaction scheme based on
736 detailed reaction mechanism. Combust Flame **162**(12), 4391–407 (2015).

737 [38] Ahmed U, Turquand d'Auzay C, Muto M, Chakraborty N, Kurose R.: Statistics of
738 reaction progress variable and mixture fraction gradients of a pulverised coal jet flame
739 using Direct Numerical Simulation data. Proc Combust Inst. **37**(3):2821–30 (2019).

740 [39] Turquand d'Auzay, C., Ahmed, U., Pillai, A.L., Chakraborty, N.: Statistics of progress
741 variable and mixture fraction gradients in an open turbulent jet spray flame. Fuel **247**,
742 198–208 (2019).

743 [40] Hu Y, Kurose R.: Nonpremixed and premixed flamelets LES of partially premixed spray
744 flames using a two-phase transport equation of progress variable. Combust Flame **188**,
745 227–242 (2018).

746 [41] Haruki, Y, Pillai, A.L., Kitano, T, Kurose, R.: Numerical investigation of flame
747   propagation in fuel droplet arrays. Atomization Sprays **28**(4), 357–388 (2018).

748 [42] Ahmed, U., Pillai, A.L., Chakraborty, N., Kurose, R.: Statistical behavior of turbulent
749   kinetic energy transport in boundary layer flashback of hydrogen-rich premixed
750   combustion. Physical Review Fluids **4**(10), 103201

751 [43] Westbrook, C.K., Dryer, F.L.: Simplified reaction mechanisms for the oxidation of
752   hydrocarbon fuels in flames. Combust Sci Technol. **27**, 31–43 (1981).

753 [44] Crowe, C.T., Sharma, M.P., Stock, D.E.: The particle-source-in cell (PSI-CELL) model
754   for gas-droplet flows. J. Fluids Eng. **99**, 325–32 (1977).

755 [45] Bellan, J., Summerfield, M.: Theoretical examination of assumptions commonly used for
756   the gas phase surrounding a burning droplet. Combust Flame **33**, 107–22 (1978).

757 [46] Bellan, J., Harstad, K.: Analysis of the convective evaporation of nondilute clusters of
758   drops. Int. J. Heat Mass Trans. **30**(1), 125–36 (1987).

759 [47] Miller, R.S., Harstad, K., Bellan, J.: Evaluation of equilibrium and non-equilibrium
760   evaporation models for many-droplet gas-liquid flow simulations. Int. J. Multiphase
761   Flow **24**(6), 1025–55 (1998).

762 [48] Miller, R.S., Bellan, J.: Direct numerical simulation of a confined three-dimensional gas
763   mixing layer with one evaporating hydrocarbon-droplet laden stream. J. Fluid Mech. **384**,
764   293–338 (1999).

765 [49] Grosshandler, W,L.: RADCAL: a narrow-band model for radiation calculations in a
766   combustion environment. NIST Technical Note 1402, (1993).

767 [50] Barlow, R.S., Karpetis, A.N., Frank, J.H., Chen, J-Y.: Scalar profiles and NO formation
768   in laminar opposed-flow partially premixed methane/air flames. Combust. Flame **127**,
769   2102–2118 (2001).

770 [51] Bilger, R.: Turbulent flows with nonpremixed reactants. In: Libby P, Williams F, editors.
771   Turbulent reacting flows. Top. Appl. Phys. vol. 44. Berlin/ Heidelberg: Springer; 1980.
772   p. 65–113.

773 [52] Wandel, A.P.: Extinction predictors in turbulent sprays. Proc Combust Inst **34**, 1625–
774   1632 (2013).

775 [53] Wandel, A. P.: Influence of scalar dissipation on flame success in turbulent sprays with
776   spark ignition. Combust Flame **161**(10), 2579–2600 (2014).

777 [54] Bray, K.N.C., Domingo, P., Vervisch, L.: Role of the progress variable in models for
778   partially premixed turbulent combustion. Combust. Flame **431-437**, 141 (2005).

779 [55] Malkeson, S.P., Chakraborty, N.: Statistical analysis of displacement speed in turbulent
780   stratified flames: A Direct Numerical Simulation study. Combust. Sci. Technol. **182**,
781   1841–1883 (2010).

782 [56] Peters, N., Terhoeven, P., Chen, J.H., and Echekki, T.: Statistics of Flame Displacement
783   Speeds from Computations of 2-D Unsteady Methane-Air Flames, Proc. Combust. Inst.,
784   **27**, 833-839 (1998).

785 [57] Echekki, T., Chen, J. H.: Analysis of the contribution of curvature to premixed flame
786   propagation, Combust. Flame, **118**, 303-311 (1999).

787 [58] de Chaisemartin, S., Fréret, L., Kah, D., Laurent, F., Fox, R., Reveillon, J., Massot, M.:
788   Eulerian models for turbulent spray combustion with polydispersity and droplet crossing.
789   Comptes Rendus Mécanique 337(6–7), 438–448 (2009).

790 [59] Pope, S.: Turbulent flows. Cambridge University Press; 2000.

791 [60] Yamashita, H., Shimada, M., Takeno, T.: A numerical study on flame stability at the
792   transition point of jet diffusion flames. Proc. Combust. Inst. **26**, 27–34 (1996)

793 [61] Wang, H., Hawkes, E.R., Chen, J.H., Zhou, B., Li, Z., Aldén, M.: Direct numerical
794   simulations of a high Karlovitz number laboratory premixed jet flame – an analysis of
795   flame stretch and flame thickening. J. Fluid Mech. **815**, 511-536 (2017).

796 [62] Trouvé, A., Poinsot, T.J.: The evolution equation for the flame surface density in
797   turbulent premixed combustion. J. Fluid Mech. **278**, 1-31 (1994).

798 [63] Boger, M., Veynante, D., Boughanem, H., Trouve, A.: Direct numerical simulation
799   analysis of flame surface density concept for large eddy simulation of turbulent premixed
800   combustion. Proc. Combust. Inst. **27**, 917-925 (1998).

801 [64] Malkeson, S.P., Chakraborty, N.: Statistical analysis and a-priori modelling of flame
802   surface density transport in turbulent stratified flames: A Direct Numerical Simulation
803   study, Flow Turb. Combust., **90**, 143-187 (2013).